Climate Dynamics (2001) 17: 339–359

M. Rummukainen · J. Räisänen · B. Bringfelt
A. Ullerstig · A. Omstedt · U. Willén
U. Hansson · C. Jones

A regional climate model for northern Europe: model description and results from the downscaling of two GCM control simulations

Received: 10 December 1999 / Accepted: 5 June 2000

Abstract This work presents a regional climate model, the Rossby Centre regional Atmospheric model (RCA1), recently developed from the High Resolution Limited Area Model (HIRLAM). The changes in the HIRLAM parametrizations, necessary for climate-length integrations, are described. A regional Baltic Sea ocean model and a modeling system for the Nordic inland lake systems have been coupled with RCA1. The coupled system has been used to downscale 10-year time slices from two different general circulation model (GCM) simulations to provide high-resolution regional interpretation of large-scale modeling. A selection of the results from the control runs, i.e. the present-day climate simulations, are presented: large-scale free atmospheric fields, the surface temperature and precipitation results and results for the on-line simulated regional ocean and lake surface climates. The regional model modifies the surface climate description compared to the GCM simulations, but it is also substantially affected by the biases in the GCM simulations. The regional model also improves the representation of the regional ocean and the inland lakes, compared to the GCM results.

1 Introduction

The basic tools to generate climate scenarios for the future are general circulation models (GCM). They are used to simulate the global climate system and its evolution due to estimated anthropogenic forcing. Due to the global scope and long time periods involved, only a relatively coarse spatial resolution is used in GCMs. The projections of global mean warming by year 2100, compared to the present-day, as a consequence of anthropogenic emission of greenhouse gases to the atmosphere, range from 1 to 3.5 °C (Houghton et al. 1996). The global change would be a sum of regional changes scattering on both sides of the global mean. There is a serious shortfall in simulations on the regional and local scales where the most detailed impact analyses are made.

Various techniques exist (Giorgi and Mearns 1991) to add detail to the large-scale global climate model results, known collectively as downscaling or regionalization. They account for effects on scales that are not represented in large-scale global models and can add significant detail on the climate scenarios. Most of the approaches fall into one of the two categories statistical downscaling (for a recent summary, see Rummukainen 1997) or dynamical downscaling. In the former, relationships between large-scale climate variables and local surface climate variables are established and calibrated using long time series of observations. These relations are then used to compute local variables from GCM-generated large-scale fields. The statistical techniques are inexpensive, but also inherently limited by their explicit link to past climate statistics.

Dynamical downscaling involves the use of regional climate models (RCM) with time-dependent boundary conditions taken from GCM results. Physical interactions and possible non-linear feedback are therefore included in the interpretation. Regional climate modeling is related to, but not analogous with, (weather) forecast use of limited area models. In the former, the boundary forcing and the regional model parametrizations govern the solution. In the latter, besides the regional model parametrizations, the initialization and often also data assimilation are important.

The idea of regional climate modeling was presented by Dickinson et al. (1989). The first month-long simulations were done by Giorgi and Bates (1989), and the first multi-year simulation by Giorgi et al. (1994). Useful reviews on regional climate modeling are given by

M. Rummukainen (✉) · J. Räisänen · B. Bringfelt · A. Ullerstig
A. Omstedt · U. Willén · U. Hansson · C. Jones
Rossby Centre, Swedish Meteorological and
Hydrological Institute, SE-60176 Norrköping, Sweden
E-mail: markku.rummukainen@smhi.se

Also at:
A. Omstedt
Department of Earth Sciences, University of Göteborg, Sweden

Giorgi and Mearns (1991, 1999), Houghton et al. (1996) and McGregor (1997). A number of specific RCMs are described by Giorgi et al. (1993a, b), Giorgi and Mearns (1999), Laprise et al. (1998), McGregor and Walsh (1994), Sasaki et al. (1995), Jones et al. (1995), Christensen et al. (1997, 1998), Jacob and Podzun (1997), and Machenhauer et al. (1996, 1998).

Here we describe an RCM for the northern Europe region. It is version 1 of the Rossby Centre regional Atmospheric climate model (RCA1). RCA1 is the key tool in the Swedish regional Climate Modelling programme, SWECLIM. The program objective is to provide regional interpretation of global climate (change) scenarios, to be used in regional impact studies. Here, RCA1 results from two control runs are presented. The RCA1 model is described in Sect. 2–3. The results from two 10-year downscaling exercises, at a relatively coarse regional model resolution for a 'control' ($\sim$ present-day) climate, are discussed in Sect. 4. The concluding summary is given in Sect. 5. Analysis of the simulated hydrological cycle and regional climate scenario results will be reported in forthcoming papers.

2 Model design and simulation set-up

2.1 Model parametrizations: general

RCA1 is based on the operational limited area forecast model HIRLAM (Källén 1996; Eerola et al. 1997). It is a hydrostatic, primitive equation gridpoint model with Eulerian advection and a leapfrog semi-implicit time integration (Simmons and Burridge 1981). The prognostic variables are temperature, specific humidity, horizontal wind, cloud water and surface pressure. Cloud ice is diagnostic. Except for the advection of cloud water, second order centered finite difference approximations are used. Cloud water is transported by an upstream scheme. Horizontal diffusion is performed with a linear fourth-order scheme. Additional prognostic variables are snow cover, soil temperature and soil moisture. The surface/soil/snow scheme has been further modified from the HIRLAM one (see Sect. 3.1), but the soil scheme is still forced from below by prescribed deep soil temperatures. In HIRLAM, SSTs and ice are prescribed. In RCA1, however, SSTs and ice are calculated prognostically (see Sect. 3.2–3.3) for the Baltic Sea and the lakes in the Baltic Sea catchment region. The North Atlantic SSTs and ice are prescribed even in RCA1.

Those HIRLAM parametrizations that are retained in RCA1 reflect the legacy of the model in forecasting; they include the radiation scheme from Savijärvi (1990) and Sass et al. (1994), the slightly modified Kuo (1965, 1974) convection scheme, the large-scale cloud and precipitation microphysics from Sundqvist et al. (1989) and Sundqvist (1993) and the first-order vertical diffusion scheme of Louis (1979) including modifications of Geleyn (1987). This combination of the parametrizations implemented in HIRLAM is well-tested for short-range forecasting.

The HIRLAM radiation scheme has two spectral ranges, one for shortwave and one for the longwave. Radiative transfer depends on the prognostic water vapor and cloud fields. The roles of CO_2, ozone and background aerosol are incorporated as constants and there is no explicit allowance for a changing CO_2. These constants have been used even in RCA1. This fixed-CO_2 treatment may seem a limitation in climate applications. At least regarding the temperature, however, the CO_2 concentration in RCA1 is relatively unimportant, because the model is strongly forced by the driving GCM from the lateral boundaries, by the Atlantic SSTs and the deep soil temperature. Indeed, in the first RCA1 climate scenario experiments (manuscript in preparation), only slightly smaller temperature changes were obtained than in the driving GCMs. More recently, the model has also been run with a modified radiation scheme that allows for varying CO_2 (Räisänen et al. 2000). Two integrations were made using the same boundary forcing. In one of the integrations, the present-day CO_2 concentration was used. In the other integration, the CO_2 concentration was doubled. The results from these were separated by less than 0.2 °C in the land area mean surface air temperature. Aloft the differences were even smaller.

In the vertical diffusion and surface schemes, some subgridscale effects are included. The roughness lengths, surface exchanges and diagnostic near-surface variables are calculated separately for a land fraction and a water fraction in each grid box. When sea ice is present, the appropriate fraction of a grid box is treated as land. The roughness lengths are the same for the momentum, heat and moisture exchanges. Over land, they include an orographic input and one for vegetation and are invariant in time. Over water, they are calculated from the local wind speed using the Charnock formula.

A Davies-type (Davies 1976) boundary relaxation is applied on surface pressure, temperature, specific humidity, wind and cloud water, with a *tanh*-shape weight function in an 8-point wide boundary zone.

2.2 Model domain and resolution

The RCA1 domain is set with a spherical, rotated latitude/longitude Arakawa C grid. There are 19 vertical levels. The hybrid vertical coordinate is from Simmons and Burridge (1981). The model top is at 10 hPa. Here, simulations with a relatively coarse 88 km horizontal resolution with the forcing from two different GCMs are reported.

The driving GCM data are from a 10-year time slice from the control run of the UKMO HadCM2 GCM (Johns et al. 1997) with constant greenhouse gases (GHG), and from a 10-year time slice of a transient GHG scenario run from the ECHAM4/OPYC3 GCM of the Max Planck Institute for Meteorology in Hamburg (Roeckner et al. 1996a, b, 1999; Oberhuber 1993). This ECHAM4 run was started nominally at 1860, but from present-day atmospheric GHG levels used in a long control simulation. Our time slice is centered at the model year 1990. During the preceding 130-year period, the GHG concentrations were increased by 26% (as expressed in equivalent CO_2) to provide for the observed radiative forcing history. The 10-year time-slice has, therefore, almost 1 °C higher global mean temperature than the unperturbed ECHAM4/OPYC3 control run (see Machenhauer et al. 1998, Fig. 0.3).

These GCMs include fully three-dimensional components for both the atmosphere and the oceans. HadCM2 is a grid point model with a resolution of 2.5° in latitude and 3.75° in longitude. The ECHAM4 atmospheric dynamics are represented in spectral space with a T42 truncation and a transform grid with a resolution of about 2.8° by 2.8°.

Hereafter the downscaling of the ECHAM4 (HadCM2) simulation is called RCA-E (RCA-H). Of these, the RCA-H was computed first. A slightly larger domain for the RCA-E experiment was found necessary as the combination of ECHAM4 and RCA1 produced a very marked boundary problem in precipitation (see Sect. 4.2). The domains used are shown in Fig. 1.

3 Modifications to the HIRLAM parametrizations

Källén (1996) gives a description of the parent HIRLAM model. Rummukainen et al. (1998) describe the earlier, test version of the RCA1 model. The original land surface and snow schemes and the treatment of the regional ocean and lakes have been further modified in RCA1. These changes are discussed later.

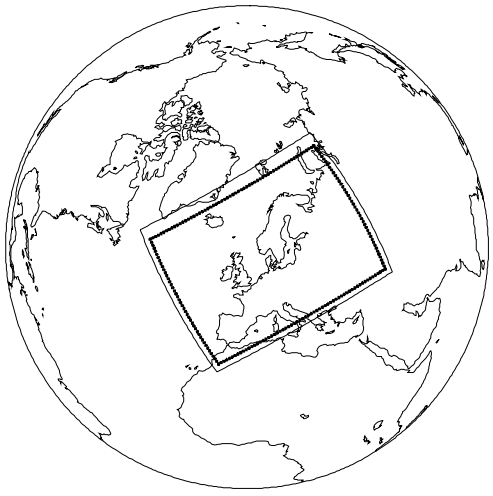

Fig. 1 RCA1 domains. The *outer* (*inner*) one is used with the ECHAM4/OPYC3 (HadCM2) driving

3.1 Land surface parametrization

In HIRLAM, the soil temperature and moisture evolution are constrained by a relaxation to prescribed deep-soil fields. In RCA1, this is done for the deep soil temperature, relaxing it to the deep-soil evolution in the driving GCM. There are two prognostic soil temperature layers (7.2 and 43.2 cm thick). The top layer accommodates even the snow cover. The third soil temperature layer carries the prescribed deep-soil field. For soil moisture in RCA1, relaxation is not used. There are two prognostic soil moisture layers (7.2 and 80 cm thick). The total soil column water holding capacity equals 242 mm.

In RCA1, hydraulic and thermal diffusivities vary with soil texture and soil moisture (Clapp and Hornberger 1978; McCumber and Pielke 1981). Surface forcing is by vertical fluxes of heat in the case of temperature and by precipitation, snowmelt and evapotranspiration in the case of moisture. Heat diffusion operates between the soil temperature layers. The top layer temperature (T_s) follows the equation

$$(\rho C)_s \frac{\partial T_s}{\partial t} = \sum_i \Phi_i + \frac{\partial}{\partial z}\left(\lambda_T \frac{\partial T}{\partial z}\right)_s \tag{1}$$

Φ_i lists the surface heat flux components, λ_T is soil thermal conductivity [W m^{-1} K^{-1}] and ρC is the volumetric soil heat capacity [J m^{-3} K^{-1}]. In the second soil temperature layer, the soil freezing from Viterbo et al. (1999) is used. Soil freezing acts to increase soil heat capacity, and delays soil freezing/melting in autumn/spring. The heat from soil freezing, $L\rho_w(\partial\theta/\partial t)$ [W m^{-3}], appears in the equation for the second soil layer temperature (T_d)

$$(\rho C)_d \frac{\partial T_d}{\partial t} = L_i \rho_w \left(\frac{\partial \theta}{\partial t}\right)_d + \frac{\partial}{\partial z}\left(\lambda_T \frac{\partial T}{\partial z}\right)_d \tag{2}$$

where z is the vertical coordinate, L_i is the latent heat of freezing/melting [J kg^{-1}] and ρ_w is the density of water. The vertical transport term in Eq. (2) includes contributions from interaction with the layer above and the relaxation to the prescribed layer below. The dimensionless frozen soil water amount θ is proportional to the corresponding field capacity soil water amount, i.e., $\theta = \theta_{FC} f(T)$, to prevent undesirable coupling between the temperature and moisture equations. The fraction of water in the ice phase, $f(T)$, is unity at soil temperatures below $-3\,^\circ$C, zero at soil temperatures above $+1\,^\circ$C and follows a *sin*-relationship in between.

Soil moisture transfer includes Darcian flow and runoff is routed down the soil column as in the hydrological HBV model (Lindström et al. 1997). Soil moisture loss by evapotranspiration is partitioned between the two soil moisture layers according to transpiration via vegetation after the ISBA model (Noilhan and Planton 1989).

Snow depth is accumulated by snowfall (P_S) and depleted by snow melt (S_M) and evaporation (E_S). Snow melt operates whenever the gridbox average surface temperature is above the melting temperature. S_M is proportional to the number of degrees above the melting temperature, accounting for the snow amount and its thermal characteristics. The snow melt term enters the top layer soil moisture (w_s) equation as well:

$$\frac{\partial w_s}{\partial t} = \lambda\left(\frac{\partial w}{\partial z}\right) + P_R + S_M - E_{act}(1 - p_{tr}) - Q_1 \tag{3}$$

where λ is the hydraulic conductivity, P_R is the rainfall rate, E_{act} is the rate of actual evapotranspiration from snow free surface and p_{tr} gives the fraction of it used for transpiration. The second layer soil moisture (w_d) evolves according to:

$$\frac{\partial w_d}{\partial t} = -\lambda\left(\frac{\partial w}{\partial z}\right) - E_{act} p_{tr} + Q_1 - Q_2 \tag{4}$$

Drainage from the top layer to the second layer (Q_1) and runoff from the second layer (Q_2) operate whenever there is precipitation or snow melt. The partitioning of the water input between moistening the soil and runoff depends on the soil moisture content. The runoff occurs in two steps. The first step brings water from the top layer to the second layer. The second step dislocates water from the second layer and away from the model. The runoff formulation has an in-built stabilizing effect on soil moisture. When soil moisture is high (low), runoff for a given precipitation and/or snow melt is great (small) and soil moisture increases by a small (large) amount:

$$Q_1 = (P_R + S_M) \cdot \left(\frac{w_s}{w_{FC}}\right)^{\beta_1} \tag{5a}$$

$$Q_2 = Q_1 \cdot \left(\frac{w_d}{w_{FC}}\right)^{\beta_2} \tag{5b}$$

The rightmost terms, with the exponents $\beta_1 = \beta_2 = 2$, relate to subgridscale variability in soil moisture (see Bergström and Graham 1998), indicating how large a fraction of a gridbox has runoff when its mean moisture content is below field capacity.

The actual evapotranspiration (E_{act}) is calculated as the fraction α of the potential evapotranspiration E_{pot}. The α is given in terms of the aerodynamic and surface resistances. E_{pot} is as calculated for a wet surface, using saturation specific humidity at surface temperature $q_{sat}(T_s)$ [kg kg^{-1}], specific humidity at the lowest model level q_a and air density ρ. The following apply:

$$\alpha = \frac{r_s}{r_s + r_a} = \left(1 + \frac{r_s}{r_a}\right)^{-1} \quad \text{and} \quad E_{pot} = \rho \frac{q_{sat}(T_s) - q_a}{r_a} \tag{6}$$

where r_a [s m^{-1}] is the aerodynamic resistance and r_s is the total surface resistance ($r_s = 0$ for a wet surface). Their ratio depends on air temperature and soil water stress (F_4 and F_2, see later), as:

$$r_s = r_{sNOTR} \cdot \min\left(1, \frac{F_4}{F_2}\right) \tag{7}$$

where r_{sNOTR} is the top layer resistance in absence of vegetation effects. It is an empirical function of top layer soil moisture and if the top soil layer is very dry ($w_s/w_{FC} \leq 0.05$), evaporation is prevented from exceeding the available soil moisture amount:

$$\left(1 + \frac{r_{sNOTR}}{r_a}\right)^{-1} = \min\left[0.05 + 0.95\left(\frac{w_s}{w_{FC}}\right)^8, \frac{w_s}{w_{FC}}\right] \tag{8}$$

Outside the vegetation period, r_s is identical with r_{sNOTR}. During the vegetation period, r_s is affected by the air temperature and soil water stress. The effect of air temperature (T, [°C]) is:

$$F_4 = \min\left[1, (1 - k_0)\left(\frac{T - 25}{25}\right)^2 + k_0\right] \tag{9}$$

This is similar to the ISBA model (Noilhan and Planton 1989). The effect on vegetation transpiration is largest at 25 °C ($F_4 = k_0$) and absent at < 0 °C and at > 50 °C (in both cases, $F_4 = 1$). k_0 is the inverse of a normalized leaf area index (LAI_{norm}). Outside the vegetation period, the latter equals unity. During the vegetation period from April to October, the successive mid-month values of LAI_{norm} are 1.5, 2.5, 3, 3, 3, 2.5 and 1.5. Daily LAI_{norm} values are linearly interpolated between the monthly ones. The reduction of transpiration due to water stress (F_2) in the deep soil layer is given by:

$$F_2 = \min\left(1, \frac{w_d}{q_{sm} w_{FC}}\right) \tag{10}$$

with $q_{sm} (= 0.5)$ as the threshold for the moisture stress. Whenever the soil moisture content is >50% of the field capacity, there is no stress and transpiration occurs at the 'dry potential rate' with dry canopy but a good water supply in the root zone.

Finally, E_{act} is divided into the no-transpiration part (dries the top soil layer, see Eq. 3) and the transpiration part (dries the second soil layer, see Eq. 4), with the resistances:

$$(1 - p_{tr})E_{act} = \frac{r_s + r_a}{r_{sNOTR} + r_a} E_{act}, p_{tr} E_{act} = \frac{r_{sNOTR} - r_s}{r_{sNOTR} + r_a} E_{act} \tag{11}$$

3.2 Lake modeling

In RCA1, the Nordic lake systems are modeled with interactive lake models (Ljungemyr et al. 1996; Omstedt 1999). Data on the surface area of all lakes in the Baltic Sea catchment region is derived from geographical information. The lakes within Sweden are classified into four basic types according to their depths and areas. Three of the types differentiate between shallow lakes with mean depths < 10 m. Shallow lakes outside Sweden are represented by only one such type. The fourth basic type considers the deep lakes. They retain their individual depths and areas within and outside Sweden. The model for the deep lakes has been tested and applied also by Svensson (1978), Sahlberg (1988), Omstedt (1984) and Elo (1994).

For the shallow lakes, well-mixed conditions are assumed to hold so they are modeled 0-dimensionally. The shallow lake temperature is calculated using:

$$\frac{\mathrm{d}T_l}{\mathrm{d}t} = -\frac{1}{\rho_w c_p D}\left[\Phi_h + \Phi_e + \Phi_{lu} + \Phi_{ld} + \Phi_{sun}\right] \tag{12}$$

T_l is the lake temperature, ρ_w the water density, c_p the specific heat of water and D the lake depth. The heat fluxes, defined positive towards the atmosphere, are the sensible (Φ_h) and the latent (Φ_e) heat, the up- and downward long wave (Φ_{lu} and Φ_{ld}) and the net solar (Φ_{sun}) radiation.

In the deep lakes, vertical stratification becomes important. Thus, a 1-dimensional approach is used to vertically resolve the lake temperatures:

$$\frac{\partial T_l}{\partial t} = \frac{\partial}{\partial z}\left[\frac{\nu_T}{\sigma_T}\frac{\partial T}{\partial z}\right] + \Gamma_{sun} \tag{13}$$

where z is the vertical coordinate (positive upwards), ν_T is the kinematic eddy viscosity, σ_T is the turbulent Prandtl number and Γ_{sun} is the source term for solar radiation penetrating the water column. The net heat exchange with the atmosphere appears as a boundary condition when solving Eq. (13). The Γ_{sun} is given by:

$$\Gamma_{sun} = \frac{1}{\rho c_p}\left\{\Phi_{sun}(1-\delta)(1-A_i) + \Phi^i_{sun} A_i\right\}\beta \mathrm{e}^{-\beta(D-z)} \tag{14}$$

Φ_{sun} and Φ^i_{sun} are the short wave fluxes to the water and through the ice, respectively, A_i is the ice concentration, $1 - \delta$ is the fraction of solar radiation that penetrates into the deeper layers and β is the absorption coefficient.

For the initial ice formation, linear growth of ice thickness with time is assumed:

$$\frac{\mathrm{d}h_i}{\mathrm{d}t} = \frac{\Phi_{np}}{L_i \rho_i} \tag{15}$$

where Φ_{np} equals the net heat flux from the surface ($\Phi_n = \Phi_h + \Phi_e + \Phi_{lu} + \Phi_{ld}$) when the latter is positive. In the case of a negative Φ_{np}, it is set to zero. h_i is the ice thickness, L_i is the latent heat of freezing/melting and ρ_i is the ice density.

After the initial ice formation phase, the ice thickness grows according to:

$$\frac{\mathrm{d}h_i}{\mathrm{d}t} = \frac{k_s k_i}{(k_i h_s + k_s h_i) L_i \rho_i}\left(T_f - T_a\right) - \Phi_w \tag{16}$$

where h_s is the thickness of snow on ice, T_f is the freezing temperature of the water, T_a is the air temperature, k_s and k_i are the thermal conductivity of snow and ice and Φ_w is the heat flux from water to ice.

The melting of ice depends on the net absorbed radiation, i.e., the short-wave radiation that enters the ice surface (Φ_{st}) minus the short-wave radiation that penetrates the ice and goes into the water (Φ_{sb}):

$$\frac{\mathrm{d}h_i}{\mathrm{d}t} = \frac{\Phi_{st} - \Phi_{sb}}{\rho_i L_i} \tag{17}$$

On the shallow lakes, ice ridging is not considered. In deep lakes it is modeled by an ice front model:

$$\frac{\mathrm{d}X_f}{\mathrm{d}t} = U_i - \frac{X_f}{h_i}\frac{\Phi_n - \Phi_w}{\rho_i L_i} \quad . \tag{18}$$

X_f is the horizontal position of the ice edge and U_i is the one-dimensional ice drift. In the case of off-shore winds, the ice drift is equal to 2% of the surface wind speed (this fraction is depicted as U_i^{free}). In the case of on-shore winds, the ice drift is:

$$U_i = U_i^{free} - \frac{P_i}{X_{dim} - X_f} \tag{19}$$

where X_{dim} is the horizontal dimension of the lake and P_i is the ice strength (Hibler 1979):

$$P_i = P_* h_i \mathrm{e}^{-c_i(1-A_i)} \tag{20}$$

P_* and c_i are constants. The basic assumptions are that the ice is deformed by wind blowing towards the shore but drifting freely with off-shore winds. By modeling the ice edge, the ice concentration can be calculated and the heat fluxes calculated separately for the fraction of the lake that is ice-free ($1 - A_i$) and for the ice-covered fraction (A_i).

3.3 Baltic Sea modeling

The Baltic Sea is like a large inland sea, with a positive water balance and restricted water exchange through the narrow and shallow connections through the Skagerrak with the North Sea. The system is highly stratified through salinity. Vertical exchanges with the atmosphere and horizontal exchange through inflows and outflows need to be considered. A vertically resolved model that accounts also for horizontal advection is needed. The approach of Omstedt and Nyberg (1996), classified as a 1.5-D model, is now used in RCA1. This approach involves a division of the Baltic Sea into 13 sub-basins (Fig. 2). Between the sub-basins, horizontal exchanges are considered using geometrical and dynamic constraints, such as sounds, sills and fronts. Each sub-basin is resolved vertically, with up to 100 layers for the deepest basins. The layer depths vary from 1 m close to the surface to 10 m close to the bottom. Inflows and outflows between the basins drive the vertical advection. Omstedt and Axell (1998) show that the seasonal, interannual and longer-term variation of salinity and temperature are simulated realistically with the approach.

The equation of water temperature in each of the sub-basins reads:

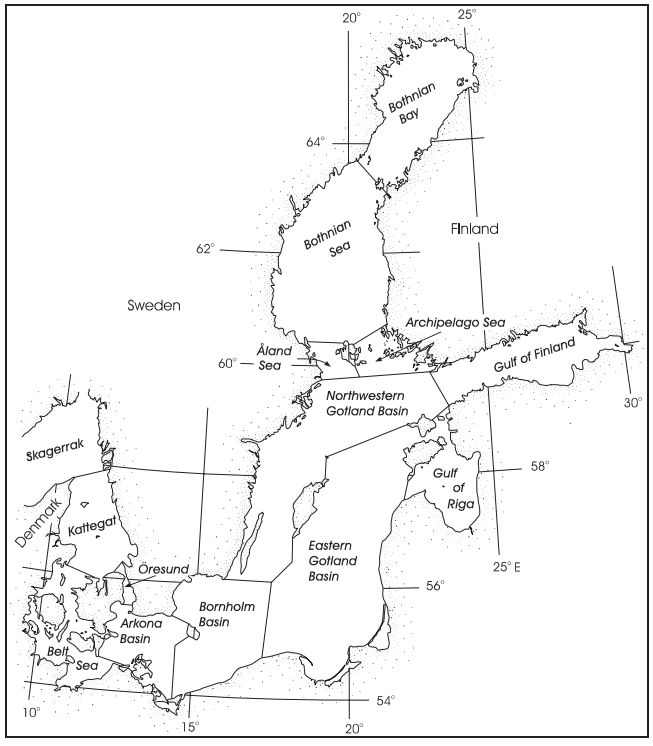

Fig. 2 The division of the Baltic Sea and Skagerrak into 13 sub-basins in the 1.5-D regional ocean model

$$\frac{\partial T_B}{\partial t} + W\frac{\partial T_B}{\partial z} = \frac{\partial}{\partial z}\left(\frac{v_T}{\sigma_T}\frac{\partial T_B}{\partial z}\right) + \Gamma_H + \Gamma_{sun} \quad . \tag{21}$$

T_B is the water temperature and W the vertical mean velocity calculated from the inflows and outflows. Γ_H is the sink/source term associated with the horizontal exchanges. Γ_{sun} is the solar radiation term. The net heat exchange with the atmosphere is used as a boundary condition. The approach resembles the model used for the deep inland lakes, but adds the term for heat associated with horizontal exchanges (*viz*. the inflows and outflows per sub-basin) and considers the vertical circulation.

The salinity (S) follows:

$$\frac{\partial S}{\partial t} + W\frac{\partial S}{\partial z} = \frac{\partial}{\partial z}\left[\frac{v_T}{\sigma_T}\frac{\partial S}{\partial z}\right] + \Gamma_S \tag{22}$$

where Γ_S is the salinity sink/source term associated with the horizontal exchanges. The net precipitation (precipitation minus evaporation) is used as a boundary condition.

Besides the equations for temperature and salinity, conservation equations for the water volume, momentum and ice are used (see Omstedt and Nyberg 1996).

In the Baltic Sea model, as well as in the model for the deep lakes, a buoyancy extended two-equation turbulence model is included. One equation is for the turbulent kinetic energy (k) and the other for its dissipation rate (ε). The deep water mixing below the thermocline or the halocline is parametrized according to Stigebrandt (1987), and verified by Omstedt and Axell (1998). The kinematic eddy viscosity, with c_μ and α as constants and N as the buoyancy frequency, reads:

$$v_T = c_\mu \frac{k^2}{\varepsilon} + \alpha\sigma_T N^{-1} \quad . \tag{23}$$

This model for the Baltic Sea considers the thermodynamic and the dynamic ice processes similarly to the model for deep lakes. In the ice front model, however, the horizontal exchanges between sub-basins are now included. The snow thickness on ice is presently taken simply as 20% of the ice thickness. (In the land points, however, snow is modeled in more detail, as briefly described in Sect. 3.1) Due to the lack of a physical model for snow on ice and changes in snow albedo (ageing), the ice covered ocean/lake albedo is fixed at a value in principle appropriate to late spring conditions of snow-free or wet ice (taken as 0.2, see Laine and Heikinheimo 1996). At the Nordic latitudes, the wintertime solar radiation is small, so in winter the results are not too sensitive to the albedo value. However, the springtime ice melt is sensitive to how the increasing solar radiation is absorbed. A low enough albedo value must be used. Analysis of the RCA1 runs suggests, however, that the 0.2 value is too low and likely initiates a too early spring melt. A more detailed modeling of snow on ice and its albedo will be pursued.

3.4 Coupling of the Baltic Sea and the lake models with the atmosphere

The lakes and the regional ocean are two-way coupled with the atmosphere in RCA1. Atmospheric forcing (2 m temperature and relative humidity, wind at 10 m height, total cloudiness, precipitation) is passed to the lake and the ocean models every six hours. These data are used in the lake models and in the Baltic Sea model to calculate the necessary fluxes (the sensible and latent heat fluxes, the net long and short wave radiation and the wind stresses) using the packages available in the water body models. Further work is underway to couple the components by only one set of fluxes. In addition, river runoff and Kattegat water level (forcing from the North Sea) are needed in the ocean model. The calculated SSTs and ice cover are returned to the atmospheric computations every six hours. The coupling follows Ljungemyr et al. (1996) and Gustafsson et al. (1998), though without data assimilation in RCA1.

Initialization of the lake models and the regional ocean model is completed with an off-line 12-month integration and multiyear weather data. As discussed by Omstedt and Rutgersson (2000), this is sufficient to cover the thermodynamic memory in the lake and Baltic Sea system, which is of the order of one year. A considerably longer integration is needed if the ocean salinity climate should be simulated in more detail, due to the longer Baltic Sea salinity stratification spin-up (Omstedt and Axell 1998).

4 Results from a 10-year control climate simulation

4.1 Driving global model data

The driving for RCA1 (lateral boundary forcing, North Atlantic SSTs and sea ice and deep soil temperature) is imported from the aforementioned two GCM simulations. The performance of these GCMs is addressed in other studies. For example, the HadCM2 control climate has been studied globally by Johns et al. (1997) and by Räisänen and Döscher (1999) for northern Europe. The ECHAM4/OPYC3 global simulations are discussed by Roeckner et al. (1996a) and for Europe in Machenhauer et al. (1998) and Christensen et al. (1998). The latter focus on a 9-year ECHAM4/OPYC3 control run time slice which is not the same as the present-day slice from the ECHAM4/OPYC3 transient GHG run used to drive RCA-E.

In general, HadCM2 and ECHAM4/OPYC3 are found to produce reasonable large-scale climate compared to ECMWF analyses (Hoskins et al. 1989), the Climate Research Unit (CRU) climatology for 1961–90 (Hulme et al. 1995), and the SST climatology of Levitus and Boyer (1994). However, looking at sub-areas of

Europe, non-negligible temperature and precipitation biases are found, which seem to be related to biases in the simulated circulation, parametrization shortcomings and the coarse GCM resolution (Machenhauer et al. 1998). In the Nordic area, one of the weaknesses of HadCM2 is a cold bias of 1–4 °C in spring and summer (Räisänen and Döscher 1999). The temperatures in ECHAM4 for the same domain are slightly above those observed. ECHAM4 also misrepresents the seasonal cycle of precipitation in the Nordic area (less precipitation in summer than in winter), and its spectral orography makes the precipitation maximum at the Scandinavian mountains diffuse. Both HadCM2 and ECHAM4 underestimate the north-south gradient in wintertime sea level pressure across Scandinavia, which indicates too weak westerly flow. Problems are likewise evident in the GCM-simulated conditions in the Baltic Sea and in the northern North Atlantic, the complete lack of ice in the Baltic Sea in HadCM2 being a striking example. Although some of the regional biases are substantial, HadCM2 and ECHAM4 seem to be among the best GCMs available and provide control climate results of reasonable quality compared with many other GCM simulations. A study of GCM runs in the CMIP2 (Coupled Model Intercomparison Project, phase 2) intercomparison suggests that most, if not all, presently used GCMs suffer from similar or worse biases in northern Europe (Räisänen 2000).

4.2 Large-scale circulation simulated in RCA1

The climate in any RCM simulation is affected by model resolution, numerical scheme and physical parametrizations and by the forcing boundary conditions. Apart from RCA1 having a higher resolution than the GCMs, the physical parametrization schemes are different. This makes it generally difficult to identify the fundamental causes of the differences between RCA1 and the driving models. Here, comparisons of RCA1 to its driving GCMs and comparisons of RCA1 and the driving GCMs to ECMWF reanalysis for 1979–1993 (ERA; Gibson et al. 1997) and the CRU climatology are discussed. To estimate the statistical significance of the differences, the t-statistic

$$t = \frac{\Delta X}{E} \tag{24}$$

is used. E is derived from interannual variability, assuming zero interannual autocorrelation. For the difference between a model and observations,

$$E = \sqrt{V_M/N_M + V_O/N_O} \tag{25}$$

V_M and V_O are the formally unbiased (“$n-1$”) interannual variances in the model simulation and in the observational data. For ERA, V_O is estimated as the average of the variances in the two RCA1 simulations, as no reanalysis data for individual years were available for this study. $N_M = 10$ for the simulations and $N_O = 14$ (30) for ERA (CRU) are the averaging periods in years. For the difference between RCA1 and the driving GCM,

$$E = \sqrt{V_{diff}/N_M} \tag{26}$$

The V_{diff} is the interannual variance of this difference. The estimates of Eqs. (25) and (26) have at least nine degrees of freedom, giving for two-sided 95% significance, a critical absolute t value of 2.262.

The 10-year means of winter (DJF) mean sea level pressure (MSLP) in the two RCA1 simulations are shown in Fig. 3a, b. Compared with ERA, the DJF distribution in RCA-H exhibits a positive bias in the northeastern part of the model domain, a negative bias in south and west, and a slightly positive bias in the southwest. This gives a too weak north-south gradient across Scandinavia and a too strong north-south gradient over southern Europe (Fig. 3c). The bias in RCA-E (Fig. 3d) is positive in most of the domain, but its pattern resembles that in RCA-H although with a slight northeastward shift and less pronounced gradients. In both RCA-H and RCA-E, there is a trough in the bias field parallel to a line extending from the British Isles towards the Caspian Sea. The biases are very similar in the driving GCM simulations (Fig. 3e–f), indicating that the biases in RCA1 are largely inherited from these. The differences between RCA1 and the driving simulations (Fig. 3g–h) are only of the order of 1 hPa, except in the northwestern part of the model domain in RCA-H and in some mountainous areas.

In summer (JJA), the overall pressure biases are smaller, and the modifications that RCA1 makes to the GCM results are in relative terms more important (Fig. 4). In RCA-H (Fig. 4c), a slight positive bias over southern Scandinavia is surrounded by negative biases in rest of the domain. This is qualitatively similar to HadCM2 (Fig. 4e), but in the central and northwestern parts of the domain the pressure in RCA-H is slightly higher (Fig. 4g). The summertime biases in RCA-E (Fig. 4d) are also generally small but, apart from the westernmost part of the regional domain, qualitatively different from those in ECHAM4 (Fig. 4f). While small negative biases dominate in ECHAM4, the biases in RCA-E are slightly positive in northern and central Europe. The difference between RCA-E and ECHAM4 (Fig. 4h) exceeds 2 hPa in much of northern Europe.

The pressure biases in RCA1 and in the driving GCMs are statistically significant in only a relatively small part of the domain. Thus, they may be substantially affected by internal variability in the simulations and in nature. The differences between RCA1 and the driving GCMs are generally more significant, even when they are smaller than the differences between the model simulations and ERA. This follows from the fact that the interannual pressure variations in RCA1 and the driving model are strongly correlated.

How the RCA1-GCM differences in time mean MSLP relate to differences in individual weather situa-

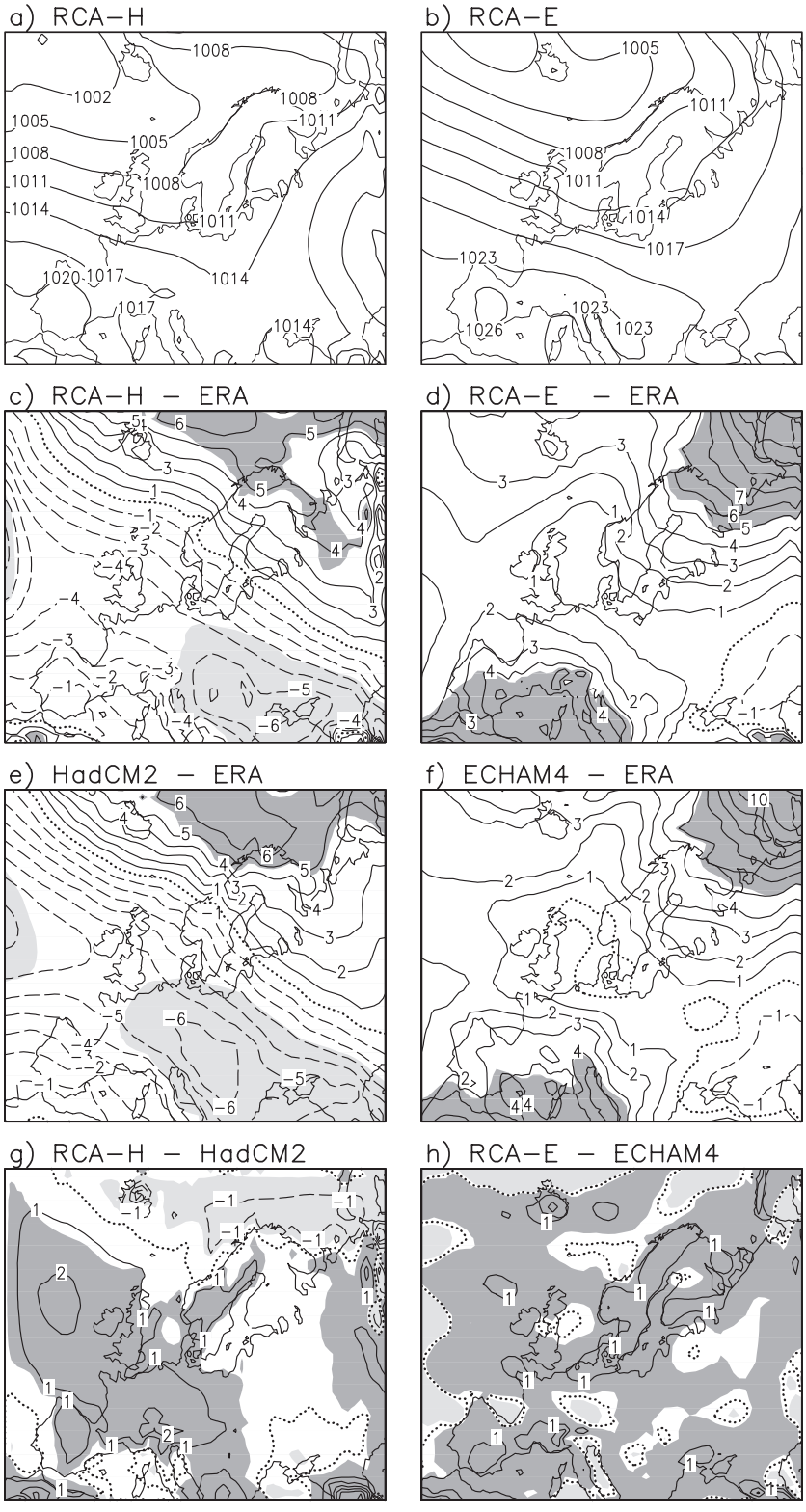

Fig. 3a–h 10-year mean winter (DJF) sea level pressure in hPa in the RCA1 simulations **a, b**, and **c, d** its bias relative to ERA for 1979–1993. **e, f** shows the bias in the driving global simulation, and **g, h** the difference between RCA1 and the driving model. The results for RCA-H and HadCM2 are shown on the *left* and those for RCA-E and ECHAM4 on the *right*. Differences significant at the 95% level are *shaded* (*dark shading* for positive and *light shading* for negative differences)

tions has not been studied for the present RCA1. An earlier version of the model showed, however, a tendency for smaller MSLP variability than the driving HadCM2 simulation with, in particular, fewer deep lows (Rummukainen et al. 1998).

The simulated tropospheric climates are characterized in Figs. 5–6 by area mean biases relative to ERA in DJF and JJA temperature and relative humidity (RH). The averaging is made in the 88 km grid over a ''common land area'' excluding the RCA1 boundary zones.

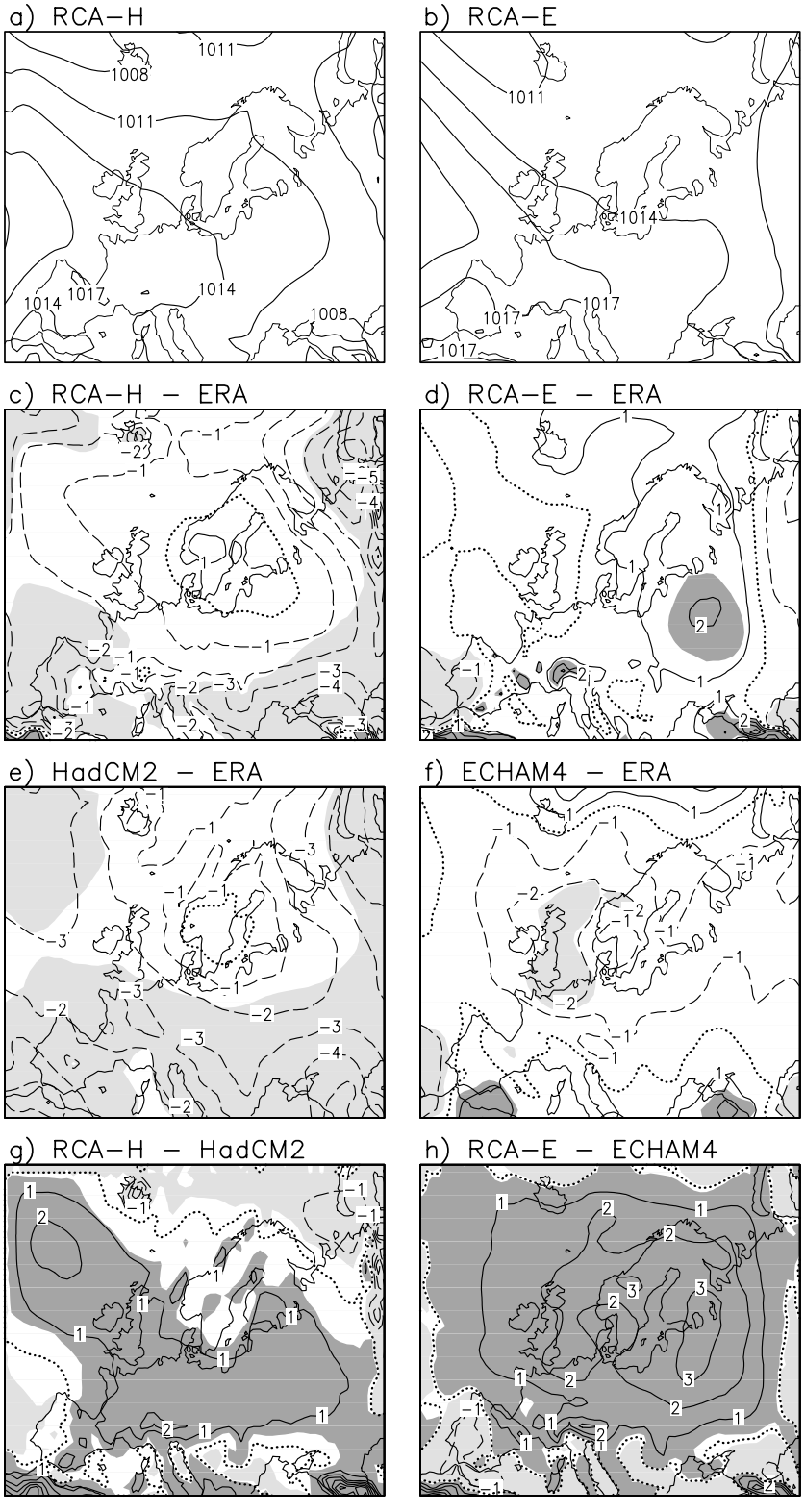

Fig. 4a–h As Fig. 3 but for summer (JJA)

Those grid boxes are included in which the land fraction exceeds 0.5 in all of RCA1, HadCM2 and ECHAM4. The two GCMs have pure land and pure sea in their own grids, but bilinear interpolation of their values to the 88 km grid yields fractional land cover. The GCM RH data have been recalculated using the RCA1 temperature-dependent combination of values with respect to water and to ice.

Area mean temperature biases (Fig. 5, left) are small in HadCM2 in DJF in the lower troposphere. The bias

grows more negative at higher levels and exceeds −4 °C above 300 hPa. A similar upward increasing cold bias also occurs in JJA (Fig. 5, middle), when a slight cold bias is present even in the lower troposphere. In contrast, the middle and lower troposphere in ECHAM4 are characterized by a small warm bias which is largest, 1–2 °C, at low levels. The sharp increase in cold bias above 300 hPa indicates a higher and colder tropopause in ECHAM4 than in ERA.

In RCA1, the lower troposphere is slightly colder than in the driving GCMs, especially in the upper part of the boundary layer at 850–925 hPa (the differences at the surface are smaller). The difference between RCA-E and ECHAM4 is larger than that between RCA-H and HadCM2 (Fig. 5, right). The lower tropospheric cooling in RCA1 over the driving GCMs is even larger in JJA than in DJF and it extends to a thicker layer. The relatively large difference between RCA-E and ECHAM4 in JJA sea level pressure (Fig. 4h) appears to be a thermal response to the colder temperatures in RCA-E, as the positive pressure anomaly in northern Europe is accompanied by a negative anomaly in geopotential heights in the upper troposphere (not shown). In winter, the temperature differences between RCA1 and the driving models are negligible at and above 500 hPa. This seasonal contrast in the differences in the vertical likely reflects, at least in part, the more efficient ventilation of the atmosphere by advection from the model boundaries in DJF and the more efficient convective mixing in JJA.

A factor that likely affects the coldness of RCA1 relative to the GCMs in JJA is the smaller amount of solar radiation absorbed in RCA1 (see Table 1). The average JJA top-of-the-atmosphere net solar radiation is in RCA-H 30 W m^{-2} smaller than in HadCM2, and in RCA-E 43 W m^{-2} smaller than in ECHAM4. There is in both cases a broad geographical similarity between the areas of largest differences in the lower tropospheric temperatures and the largest differences in the net solar radiation (not shown).

However, as RCA1 is somewhat colder than the driving models even in DJF, solar radiation can only be a part of the story. In addition, the outgoing longwave radiation is also smaller in RCA1 than in the GCMs, which actually makes the net radiative cooling of the Earth-atmosphere system in DJF smaller in RCA1 than in the GCMs. This strongly suggests that the temperature differences are also affected by processes other than radiation. Whether the differences in radiation fluxes are primarily associated with the radiation codes or with differences in simulated cloudiness and other meteorological factors requires further investigation.

Although the analyzed RH should be treated with some caution especially in the upper troposphere, both HadCM2 and ECHAM4 appear to have a positive RH bias in the RCA1 domain in DJF (Fig. 6, left). This bias increases with height in the middle and upper troposphere. Both GCMs also have a marked positive bias above 500 hPa in JJA (Fig. 6, middle). The RHs in

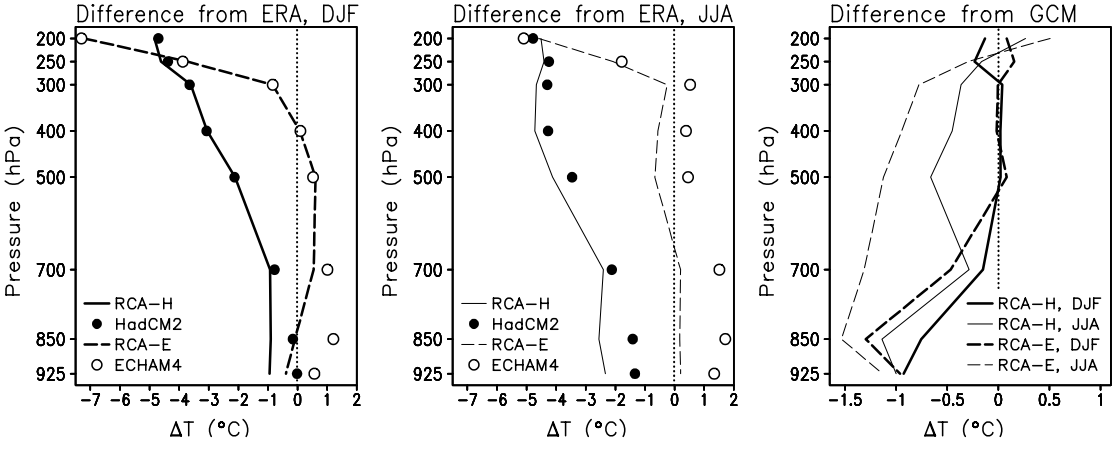

Fig. 5 10-year area mean biases of temperature relative to ERA in RCA-H, RCA-E, HadCM2 and ECHAM4 in winter (*left*) and in summer (*middle*), and the differences RCA-H – HadCM2 and RCA-E – ECHAM4 (*right*)

Table 1 Land area means of top-of-atmosphere radiation components (W m^{-2}) in DJF and JJA in the RCA1 simulations (RH = RCA-H and RE = RCA-E) and in the driving GCMs (H = HadCM2 and E = ECHAM4), and the differences between RCA1 and the driving GCM. SW is shortwave; LW is longwave; Net is LW + SW

	December–February						June–August					
	RH	H	RH-H	RE	E	RE-E	RH	H	RH-H	RE	E	RE-E
SW	43	41	2	45	47	−2	243	272	−30	250	292	−43
LW	−176	−195	19	−183	−193	10	−220	−237	17	−229	−236	7
Net	−133	−154	21	−138	−146	8	23	35	−13	20	56	−36

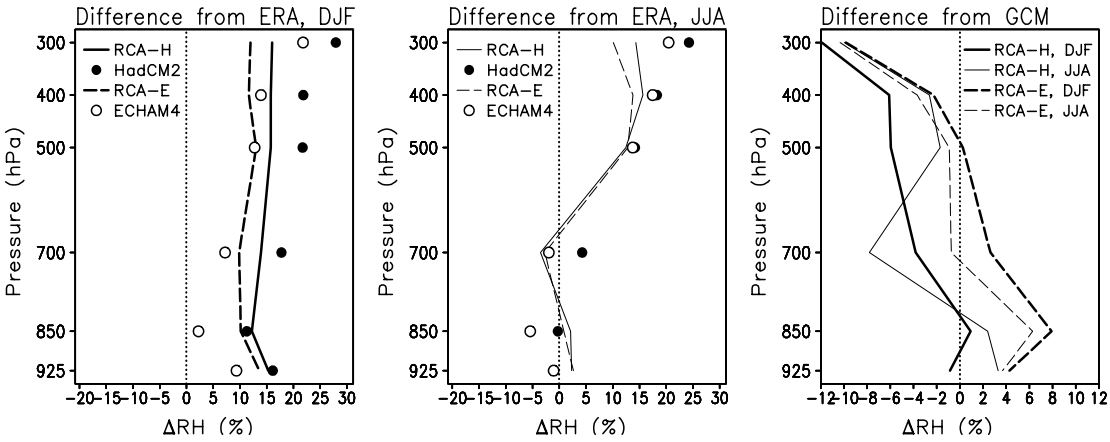

Fig. 6 As Fig. 5 but for relative humidity

ECHAM4 are generally lower (and thus the bias is less positive, or even negative in the lower troposphere in JJA) than those in HadCM2. This difference is largest in winter but it is substantial even in summer at 700 and 850 hPa. The area mean RHs in the RCA1 simulations are distinctly closer to each other than those in the driving GCMs. This indicates that RH adjusts rapidly in RCA1. The RHs in the RCA1 simulations are in both DJF and JJA close to the HadCM2 values at 850–925 hPa and closer in general to ECHAM4 in the upper troposphere, but they fall below the values in both of the two GCMs at 300 hPa.

The interpretation that RHs in RCA1 are reasonably independent from the driving model is only valid in the inner domain. Within the lateral boundary zones (excluded from the area means) and in their immediate vicinity, RCA1 is much more affected by the boundary forcing. Thus, the boundary zones are markedly (in the mid- and lower troposphere up to about 10% in the annual mean) drier in terms of RH in RCA-E than in RCA-H. This is illustrated for the 850 hPa level in Fig. 7. As a result of the lower RH, the precipitation

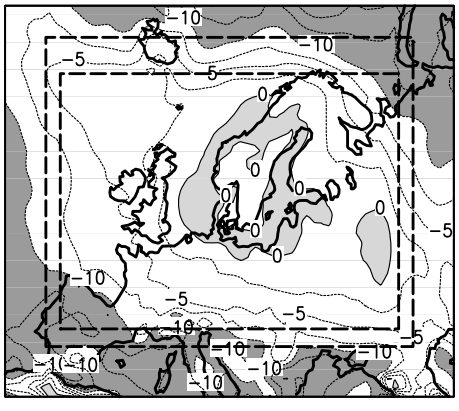

Fig. 7 Difference RCA-E – RCA-H in annual mean relative humidity at 850 hPa. Contours at every 2.5%. Values below –10% are *shaded* in *dark* and all positive values in *light*. The *thick dashed lines* indicate the inner edge of the relaxation zones in RCA-H (*inner*) and RCA-E (*outer*)

in the RCA-E boundary zones is very small with sharp gradients inwards (see Fig. 11). The widening of the model area in RCA-E over that used in RCA-H was motivated by the need to keep these gradients away from the Nordic area.

The lack of precipitation in the RCA-E boundary zones indicates a discrepancy between the moist physics of RCA1 and ECHAM4. ECHAM4 tends to remove the water from the atmosphere as precipitation at comparably low RHs, producing an atmosphere that is too dry for the formation of precipitation in RCA1. The adjustment towards higher RHs in RCA-E could in principle follow either from an increase in absolute humidity or from a decrease in temperature. The latter pathway seems to dominate: despite the higher RHs inside the model domain (Fig. 6), RCA-E is not wetter in terms of absolute humidity than ECHAM4. In addition to radiative processes, the lack of boundary zone precipitation itself may play a role in this cooling. For example, as averaged over the western (main inflow) boundary zone, the difference in annual precipitation between RCA-E and ECHAM4 is equivalent to an almost -60 W m^{-2} difference in atmospheric condensation heating. The impact of this factor is, though, to some extent reduced by the relaxation of the boundary zone temperatures towards the driving GCM.

The local differences between the various simulations and from ERA are quantified in Table 2 using root-mean-square (rms) values for the common land area. A selection of parameters characterizing the DJF and JJA conditions in the lower troposphere (MSLP and temperature, RH and zonal wind at 850 hPa) and in the upper troposphere (geopotential height, temperature, RH and zonal wind at 300 hPa) are included.

There is no systematic tendency of RCA1 either to reduce or to worsen the biases in the driving GCM simulations. For most of the parameters included, however, the root-mean-square (rms) errors are somewhat smaller for RCA-E than for RCA-H. The differences between RCA1 and the driving GCMs are in most cases small compared with the original GCM biases. As normalized by a collective rms error of the two GCMs ($[(\mathrm{rms}^2(\mathrm{HadCM2\text{-}ERA}) + \mathrm{rms}^2(\mathrm{ECHAM\text{-}ERA}))/2]^{1/2}$)

Table 2 Root-mean-square (rms) errors relative to ERA in the HadCM2 (H), RCA-H (RH), ECHAM4 (E), and RCA-E (RE) runs, and rms differences between some of these. The differences between RCA and the driving GCMs (RCA-H – H, RCA-E – E) are also given as normalized by the collective rms error of the two GCMs. Results are shown for MSLP, 300 hPa geopotential height (*Z*300), temperature (*T*850 and *T*300), relative humidity (*RH*850 and *RH*300) and the zonal wind component (*U*850 and *U*300) at 850 and 300 hPa. The calculation is made over the common land area

		H-ERA	*RH*-ERA	*E*-ERA	*RE*-ERA	*RH-H* (norm)	*RE-E* (norm)	*H*-E	*RH*-RE
MSLP (hPa)	DJF	3.9	3.4	2.3	2.9	0.9 (0.30)	0.7 (0.23)	4.6	4.2
	JJA	2.2	1.3	1.1	1.2	1.1 (0.67)	2.1 (1.23)	1.7	2.1
*Z*300 (m)	DJF	83	91	34	30	8.8 (0.14)	5.9 (0.09)	113	115
	JJA	130	143	32	26	17 (0.18)	28 (0.29)	152	141
*T*850 (°C)	DJF	0.8	1.2	1.6	1.0	0.8 (0.60)	1.3 (1.02)	1.9	1.5
	JJA	2.3	3.0	1.7	0.8	1.2 (0.59)	1.7 (0.82)	3.5	3.0
*T*300 (°C)	DJF	3.7	3.6	1.2	1.2	0.2 (0.07)	0.1 (0.02)	3.0	2.9
	JJA	4.3	4.6	1.2	1.3	0.4 (0.11)	0.8 (0.26)	5.0	4.6
*RH*850 (%)	DJF	13.8	14.5	5.9	11.7	2.7 (0.25)	8.2 (0.78)	9.9	4.7
	JJA	9.0	8.8	6.7	5.7	3.5 (0.44)	7.2 (0.90)	8.3	6.3
*RH*300 (%)	DJF	28.6	16.6	22.6	13.1	12.2 (0.47)	10.0 (0.39)	6.7	5.0
	JJA	26.0	16.2	21.4	12.4	10.2 (0.43)	10.4 (0.44)	7.3	7.1
*U*850 (m/s)	DJF	2.4	2.3	1.7	1.9	0.6 (0.30)	0.6 (0.28)	2.3	2.3
	JJA	1.2	1.5	1.1	0.8	0.5 (0.47)	0.8 (0.66)	1.9	1.8
*U*300 (m/s)	DJF	2.5	2.9	3.2	3.6	0.7 (0.24)	0.6 (0.20)	2.9	3.1
	JJA	3.4	3.1	3.2	4.7	1.3 (0.40)	1.7 (0.51)	4.4	4.9

these differences vary from 0.02 (T300, RCA-E – ECHAM4 in DJF) to 1.23 (MSLP, RCA-E – ECHAM4 in JJA). In agreement with earlier studies (Jones et al. 1997; Noguer et al. 1998), the differences from the driving GCM are generally larger in summer than in winter. In addition, the normalized differences are generally larger in the lower troposphere than at 300 hPa, where strong westerly winds prevail especially in winter. In terms of temperature and RH, the RCA1 simulations are closer to each other than are the two GCMs. However, the same does not hold for the other parameters considered.

4.3 Surface air temperature and precipitation in RCA1 and the driving GCMs

Differences in annual mean temperature between the RCA1 and GCM simulations and the CRU 1961–90 climatology are shown in Fig. 8. A simple correction for orography is made with a lapse rate of 5.5 °C km^{-1} (the CRU data set itself implies a seasonally varying lapse rate of 4.9–6.0 °C km^{-1}, see Machenhauer et al. 1998). The local statistical significance, at the 95% level, of the biases (see Sect. 4.2) is also indicated. Although there are wide areas where the biases are not significant, the fraction of significant biases is generally well above the 5% on the average expected from pure chance.

Like the tropospheric temperatures (Fig. 5), the surface climate is in most of the domain colder in RCA-H (Fig. 8a) than in RCA-E (Fig. 8b). RCA-H has an annual mean cold bias of 1–2 °C in most of central Europe and in parts of the Nordic region and western Russia. A substantial warm bias occurs near the southeastern corner of the domain. In RCA-E, the annual mean temperatures are either very close to or somewhat above the climatology in almost the whole of Europe. The biases in the two RCA1 runs closely resemble those between the driving GCMs (Fig. 8c, d). With a few regional exceptions, however, RCA-H (RCA-E) is slightly colder than HadCM2 (ECHAM4) (Fig. 8e, f). The RCA1-GCM differences show in some cases sharp gradients near the coastlines, which stem from the coarse land-sea distributions in the driving GCMs.

Seasonal biases in surface air temperature in the two RCA1 runs are shown in Fig. 9. The annual cycles of the bias averaged over the common land area are shown in Fig. 10 for both RCA1 and the driving GCMs.

Temperatures in RCA-H are relatively close to CRU in winter, excluding some areas with a significant warm bias, in particular the inner parts of northern Scandinavia. The RCA-E results are broadly similar, but a significant warm bias also appears over most of the western and central Europe. In spring and summer, RCA-H is substantially too cold in most of the area, with biases below −3 °C in some parts. In spring and summer, RCA-E agrees better with the CRU data, despite a predominantly warm bias in particular in the southern part of the domain in summer. The significant cold bias in RCA-H prevails in the autumn in central Europe, whereas the bias in the northern part of the domain turns positive. The RCA-E biases in the autumn are similar, except for a smaller cold bias in central Europe.

The seasonal temperature biases in RCA1 broadly follow the biases in the driving GCMs. RCA-E is, however, almost 1 °C colder than ECHAM4 in the land area mean from May to October (Fig. 10). RCA1 thus reduces the warm summer bias in ECHAM4. The same is true for Scandinavia in winter, where the warm bias in ECHAM4 is larger than that in RCA-E. RCA-H is on the average 0.5–1 °C colder than HadCM2 from June to September. In this case, the area mean cold bias is larger in RCA-H than in HadCM2, but the difference is not

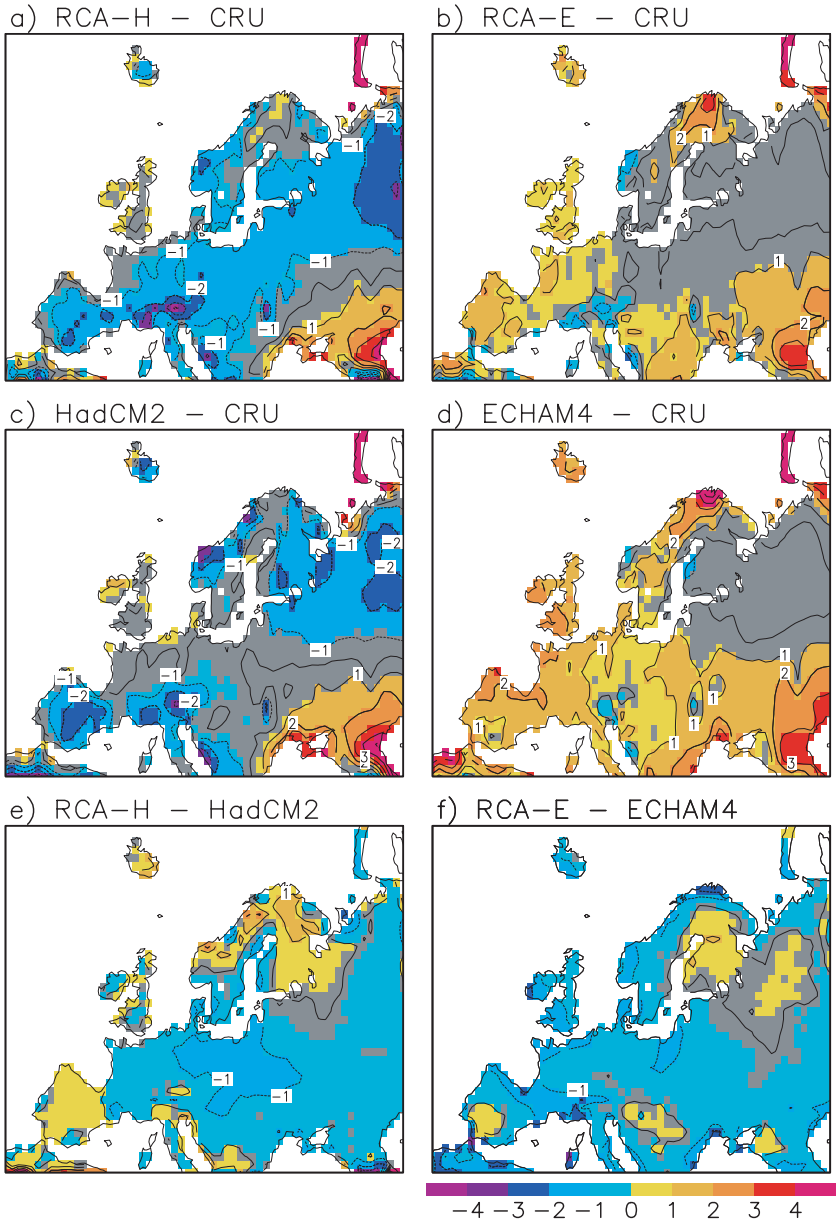

Fig. 8a–f Biases in height-corrected annual mean surface air temperature (°C) relative to the CRU climatology for 1961–90 in **a** RCA-H, **b** RCA-E, **c** HadCM2 and **d** ECHAM4, and differences **e** RCA-H – HadCM2 and **f** RCA-E – ECHAM4. The areas where the bias/difference is not at the 95% level different from zero are drawn in *gray*

geographically uniform. In the Nordic region, for example, RCA-H is slightly warmer than HadCM2 in summer.

The mean annual precipitation in the various simulations and from the CRU climatology is depicted in Fig. 11. As already mentioned, the boundary zones in RCA-E (Fig. 11b) are extremely dry. Some spurious but confined boundary features are present in RCA-H (Fig. 11a) mainly near the eastern boundary. These seem to extend a few grid points inside the relaxation zones but their impact further inside appears limited. The RCA1 simulations show qualitatively realistic geographical detail in the vicinity of high orography in the Alps, in Scotland and in Norway. Although these orographic precipitation maxima are not fully captured at the 88 km resolution, the RCA1 results are in this respect a clear improvement over the GCMs, in particular ECHAM4 with its spectrally truncated orography.

A close-up of the simulated precipitation across the highest part of the Scandinavian mountains is given in Fig. 12. The RCA-H and RCA-E simulations show qualitatively a very similar pattern of precipitation, with sharp maxima of 1960 and 2030 mm per year, respectively, just to the west of the highest orography. The greatest height of the mountains in RCA1 (at 88 km) is 1085 m, short of the true peak value of 2470 m but in good agreement with the CRU mid-level orography interpolated to the same grid. RCA1 does not, however, fully capture the sharpness and the magnitude (over 2500 mm per year in one grid box on the west coast of Norway) of the precipitation maximum indicated by CRU. The contrast to the GCM results is still evident. In

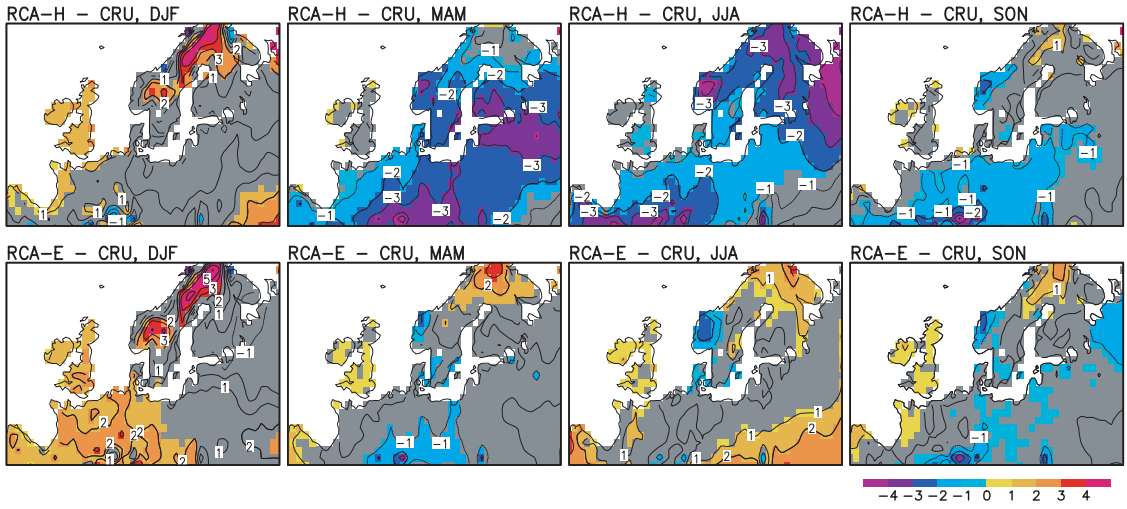

Fig. 9 Seasonal biases in height-corrected surface air temperature (°C) relative to the CRU climatology for 1961–90 in RCA-H (*top row*) and RCA-E (*bottom row*). The areas where the bias is not at the 95% level different from zero are drawn in *gray*

HadCM2, the annual precipitation maximum has a reasonable magnitude (1940 mm), but it is located just over rather than to the west of the highest HadCM2 orography of 650 m (the colored orography in Fig. 12 indicates the true size of the grid boxes in the models). The T42 spectral truncation in ECHAM4 yields a highly smoothed mountain range that has a maximum height of only 500 m and extends well over the sea in the west. Although its annual precipitation maximum (1420 mm) occurs in a realistic manner over the western slope of the orography, its location is rather away from the west coast of Norway.

In most of the domain excluding the boundary zones, the annual precipitation in all four simulations exceeds the CRU amounts. The mean difference from this in the common land area is 10% in RCA-H, 9% in RCA-E, 12% in HadCM2 and 9% in ECHAM4. Despite the similar area means, annual precipitation in RCA-E is slightly larger than that in RCA-H in most of northern and central Europe. The reverse holds near the southern edge where RCA-E still appears to be affected by the comparably low RHs supplied by ECHAM4. The bias in a Nordic region covering Norway, Sweden and Finland is 16% in RCA-H and 28% in RCA-E. The larger precipitation in the central and northern parts of the domain in RCA-E than in RCA-H may partly stem from differences in the lower tropospheric circulation. Although the MSLP tends to be in absolute terms higher in RCA-E than in RCA-H, the seasonal and annual patterns generally suggest more cyclonic flow conditions and stronger westerlies in RCA-E in central Europe. In addition, because of the higher temperatures, the absolute humidity in RCA-E generally exceeds that in RCA-H. The land mean precipitation in ECHAM4 is slightly below that in HadCM2 because of less orographic precipitation over the Alps and in Norway; in most of the remaining area the difference is reversed.

As precipitation measurements tend to underestimate the real amounts (the CRU climatology does not correct

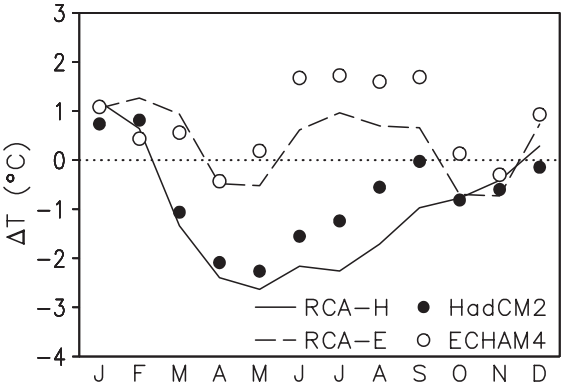

Fig. 10 Biases in the common land area mean surface air temperature (°C) relative to the CRU climatology in RCA-H (*solid line*), RCA-E (*dashed line*), HadCM2 (*solid circles*) and ECHAM4 (*open circles*)

for undercatch), the positive bias in the model simulations is at least partly fictitious. However, the difference between the observed and real precipitation is not known exactly. A recent estimate by Christensen et al. (1998, Table 8), based mainly on combining river runoff data with a model-based estimate of evaporation, suggests that the actual annual precipitation in 1961–90 exceeded the CRU data by 20% in Denmark and by as much as 47% in northern Norway. A more conservative estimate for Swedish stations (Raab and Vedin 1995) yields only a 14% difference in the annual mean but a 25–30% difference in midwinter because the dominating aerodynamic loss is larger for snow than for rain.

Seasonal precipitation biases in RCA-H and RCA-E share a number of features (Fig. 13). Precipitation in winter and spring is in most of the domain above the observed values, which, however, underestimate the real precipitation. In much of northern Europe, however, the relative bias is larger in spring than in winter, despite the fact that the measurement errors should decrease as

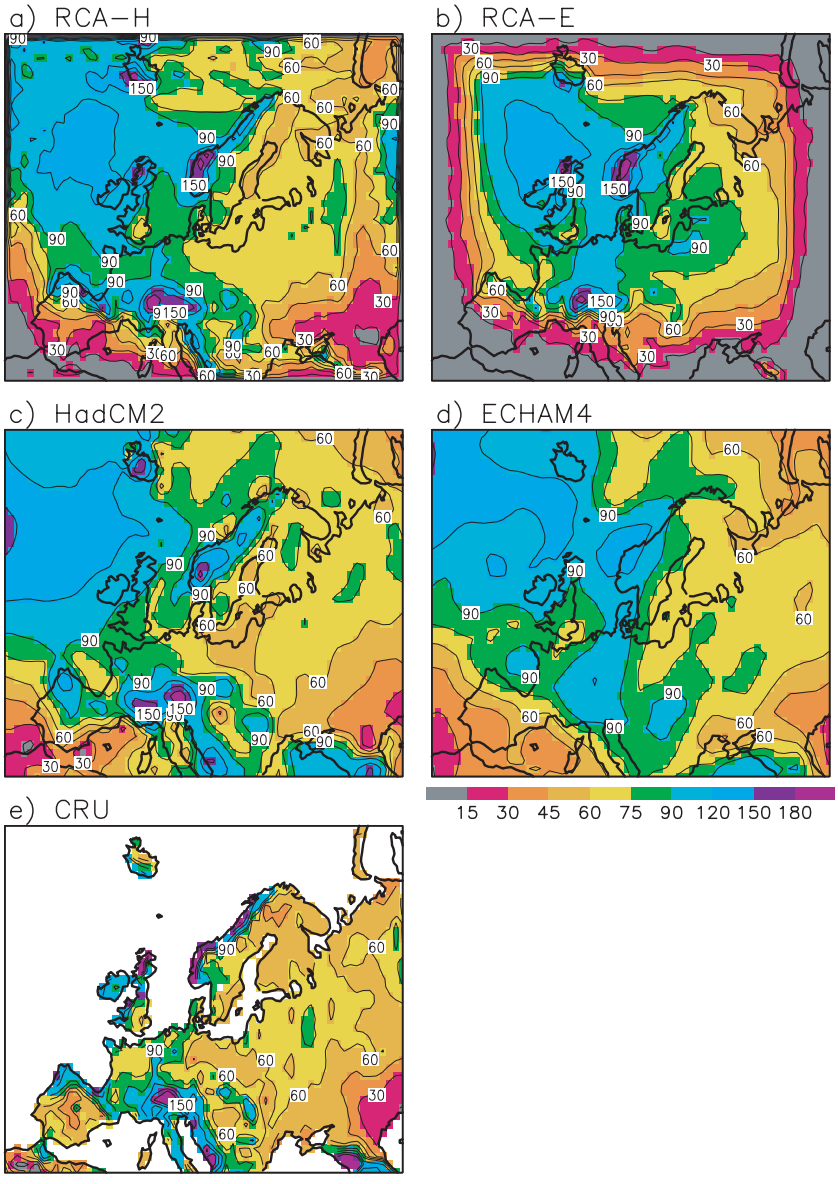

Fig. 11a–e Annual mean precipitation (cm) in the **a** RCA-H, **b** RCA-E, **c** HadCM2 and **d** ECHAM4 simulations and **e** the CRU climatology for 1961–90

the fraction of precipitation falling as snow decreases during the spring. Summer precipitation biases are in most of northern and western Europe within the uncertainty associated with the limited averaging periods, although in the southeastern part of the domain (and in RCA-E even in the southwest), summer precipitation is clearly too low. In the autumn, significant biases are predominantly positive but generally smaller than in winter and in spring.

The land area mean annual cycles in the two RCA1 simulations are generally close to the driving GCM (Fig. 14). RCA-H simulates slightly more precipitation than HadCM2 in spring and somewhat less in the summer. The 1961–90 summer maximum in precipitation is essentially absent in all cases, except for a secondary maximum in HadCM2 in June. The qualitative similarity in seasonal precipitation biases between RCA1 and the driving GCMs (not shown) holds even in most of the large-scale details. The quantitative differences are most pronounced between RCA-E and ECHAM4 in summer. The dry bias in the eastern and southern parts of the domain in summer is more pronounced in RCA-E than in ECHAM4. By contrast, ECHAM4 simulates less summer precipitation than RCA-E in northern and northwestern Europe.

A more relevant measure of model performance at the local scale than the area mean bias is the rms error. It fulfills:

$$\mathrm{rms}^2 = B^2 + D^2 \tag{27}$$

where B is the area mean bias and D^2 is the variance of bias within the area. The components of this division for seasonal and annual mean temperature and precipitation biases are given in Table 3. No correction is applied to the CRU data although this introduces a systematic error in B and some (but less predictable) error even in D.

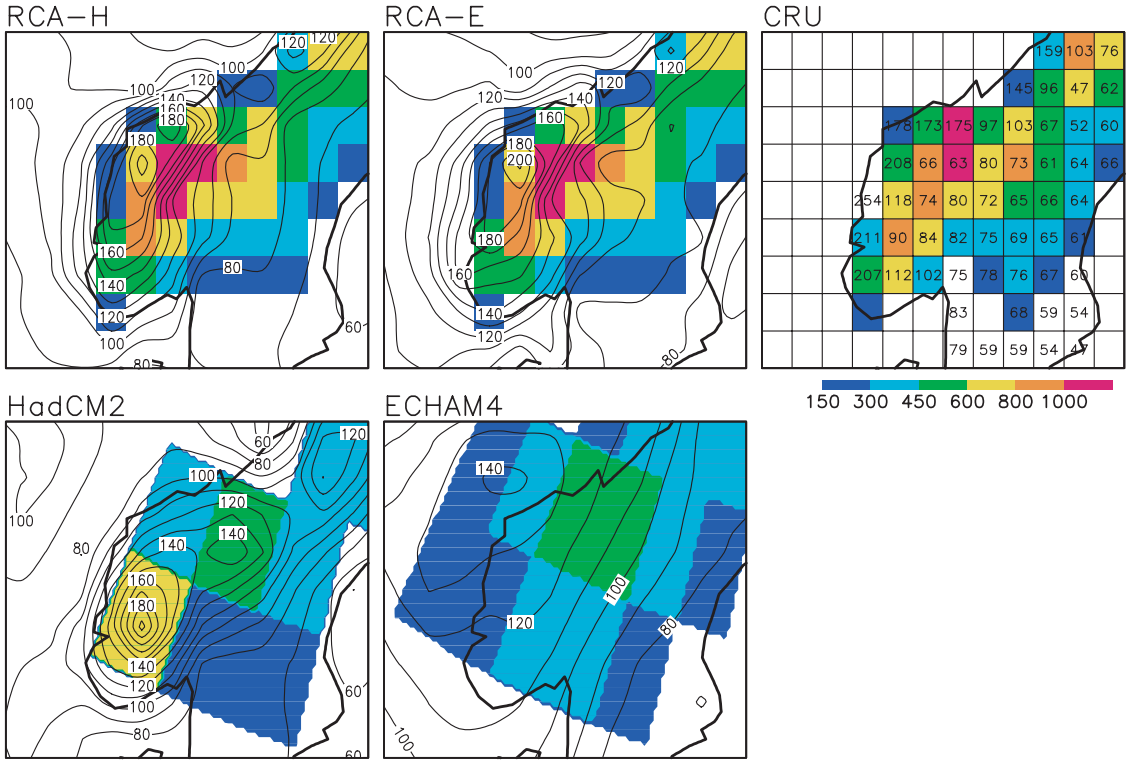

Fig. 12 Annual mean precipitation (cm; *contours* or *numeric values*) and orography (m; *color scale*) across Scandinavia in the two RCA1 simulations, in the driving GCMs and according to the CRU climatology

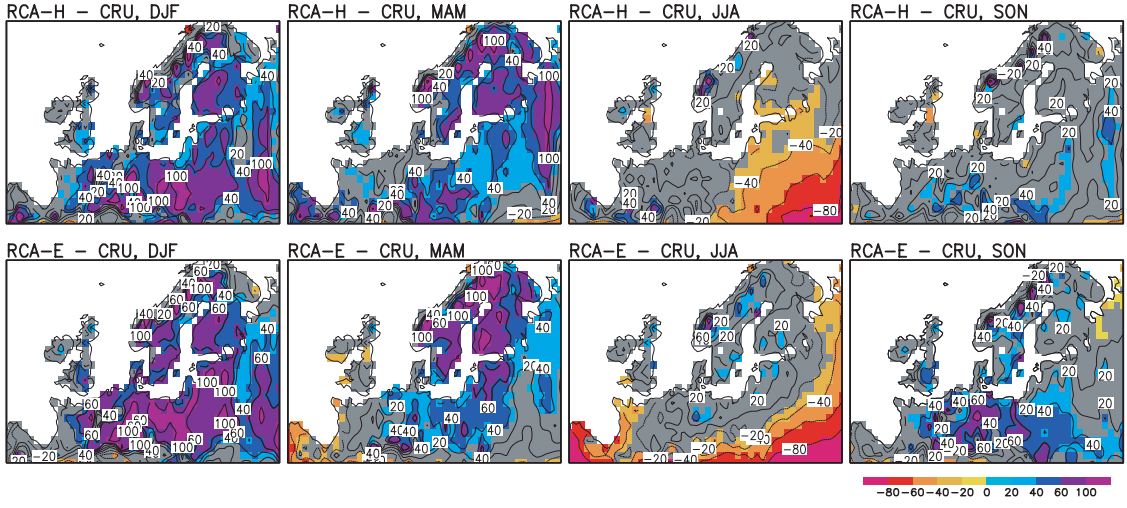

Fig. 13 Seasonal biases in precipitation (%) relative to the CRU climatology in RCA-H (*top row*) and RCA-E (*bottom row*). The areas where the bias/difference is not at the 95% level different from zero are drawn in *gray*

The local deviations have, in several cases, a larger magnitude than the area mean biases. Taking into account both temperature and precipitation, the total rms errors reveal no systematic difference in performance either between the two GCMs or the two RCA1 simulations. RCA1 has a smaller total rms error than the driving GCM in 13 of the 20 cases (two variables; two driving models; four seasons and the annual mean). The absolute value of the area mean bias is smaller in only eight cases but the distribution of temperature and precipitation within the common land area is (as indicated by *D*) better simulated than in the driving GCM with only three exceptions.

For a comparison with the results in Table 2, rms differences in temperature and precipitation between RCA1 and the driving GCMs are given in Table 4 as such and as normalized by the collective rms error of HadCM2 and ECHAM4. The normalized values vary

approximately from 0.4 to 1.0, being higher than the values for most parameters in Table 2. The impact of RCA1 on the simulated surface climate is therefore not negligible, although it is implied that a substantial reduction of the biases in the regional simulation is not possible without reducing the GCM biases. The rms differences between the two GCMs and between the two RCA1 simulations are likewise given in Table 4. Excluding spring, the differences between RCA-H and RCA-E are somewhat smaller than the differences between HadCM2 and ECHAM4.

4.4 Baltic Sea and inland lakes simulation in RCA1

4.4.1 The Baltic Sea

The Baltic Sea including the Kattegat, with an area of $\sim$420 000 km^2, is of interest even in its own right but also for its impact on climate in the surrounding areas. This sea can hardly be resolved with a typical GCM resolution (see Fig. 15). HadCM2 has a Baltic Sea of roughly the right size but its eastern arm, the Gulf of Finland, is lacking. The strongly distorted Baltic Sea in ECHAM4 actually submerges a large part of south-eastern Sweden and the whole of Denmark, and it appears more an extension of the North Sea than a separate water body. Even in RCA1 with the 88 km resolution, the geometry of the Baltic Sea is not wholly represented (however, as RCA1 allows for fractional land cover, the coastlines are in effect smoother than seen in Fig. 15). The physical properties of the Baltic Sea that directly matter for the atmosphere are the sea surface temperature (SST) and the ice cover. RCA-H and RCA-E provide a reasonable simulation of these whereas the two GCMs do not.

The average seasonal SST cycle is shown in Fig. 16 for three of the 13 basins of the Baltic Sea model in RCA1: the Bay of Bothnia in the extreme north, the Eastern Gotland Basin to the west of Latvia, and the Kattegat between Sweden and the mainland of Denmark. Compared with observations at three oceanographical stations in these basins [F9 in the Bay of Bothnia (letter 'B' in Fig. 15), BY15 in the Eastern

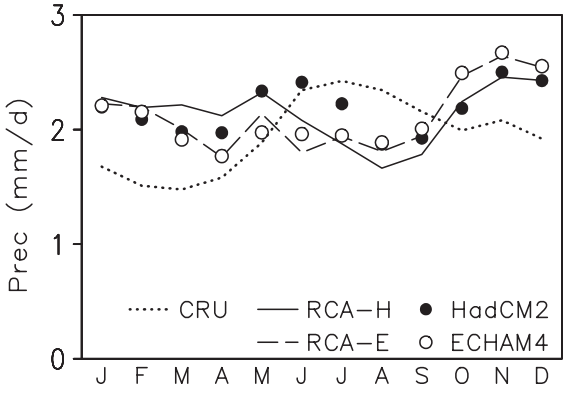

Fig. 14 Area mean precipitation (mm day^{-1}) in the common land area in the RCA-H (*solid line*), RCA-E (*dashed line*), HadCM2 (*solid circles*) and ECHAM4 (*open circles*) control runs and according to the CRU climatology (*dotted line*)

Table 4 The rms differences in surface air temperature (°C) and precipitation (% of the area mean in the CRU data) between RCA1 and the driving GCM, between the HadCM2 and ECHAM4 GCMs, and between the two RCA1 simulations. The differences between RCA1 and the driving GCM are also given as normalized by the collective rms error of the two GCM simulations (in parentheses). H is HadCM2; RH is RCA-H; E is ECHAM4; RE is RCA-E

		RH-H	*RE-E*	*H-E*	*RH-RE*
T	DJF	1.0 (0.54)	1.1 (0.60)	1.7	1.3
	MAM	0.6 (0.41)	0.7 (0.48)	2.1	2.2
	JJA	1.5 (0.68)	1.3 (0.58)	3.3	3.0
	SON	0.9 (0.81)	1.1 (1.00)	1.3	0.7
	Ann	0.8 (0.65)	0.7 (0.54)	1.8	1.6
P	DJF	33 (0.59)	28 (0.49)	34	25
	MAM	33 (0.76)	28 (0.64)	36	39
	JJA	25 (0.73)	34 (1.00)	33	30
	SON	27 (0.70)	20 (0.51)	32	24
	Ann	24 (0.72)	23 (0.67)	28	23

Table 3 Components of the division (27) for surface air temperature (*T*) and precipitation (*P*) within the common land area. The temperature values are in °C and those for precipitation in % of the area means of the CRU data set. Cases in which RCA1 is closer to CRU than the driving model are in bold. H is HadCM2; RH is RCA-H; E is ECHAM4; RE is RCA-E

		Area mean bias (*B*)				Bias deviation (*D*)				Total rms error			
		H	RH	E	RE	H	RH	E	RE	H	RH	E	RE
T	DJF	0.5	0.7	1.1	1.3	1.3	**1.2**	1.9	**1.3**	1.4	**1.4**	2.2	**1.8**
	MAM	−1.8	−2.1	0.1	**0.0**	0.8	1.0	0.9	**0.9**	2.0	2.4	1.0	**0.9**
	JJA	−1.1	−2.0	1.7	**0.8**	2.1	**1.2**	1.2	**1.0**	2.4	**2.4**	2.0	**1.2**
	SON	−0.5	−0.7	0.5	**−0.3**	1.0	**0.8**	1.0	**0.7**	1.1	1.1	1.1	**0.7**
	Ann	−0.7	−1.0	0.8	**0.4**	1.0	**0.8**	0.9	**0.7**	1.2	1.3	1.2	**0.8**
P	DJF	31	35	35	36	45	**36**	48	**41**	54	**50**	59	**55**
	MAM	27	35	14	19	35	**33**	40	40	44	48	42	45
	JJA	−8	−21	−19	−22	34	**33**	27	36	35	39	32	42
	SON	6	**4**	15	**13**	37	**27**	38	**35**	37	**27**	41	**37**
	Ann	12	**10**	9	**9**	32	**24**	32	**32**	34	**26**	34	**33**

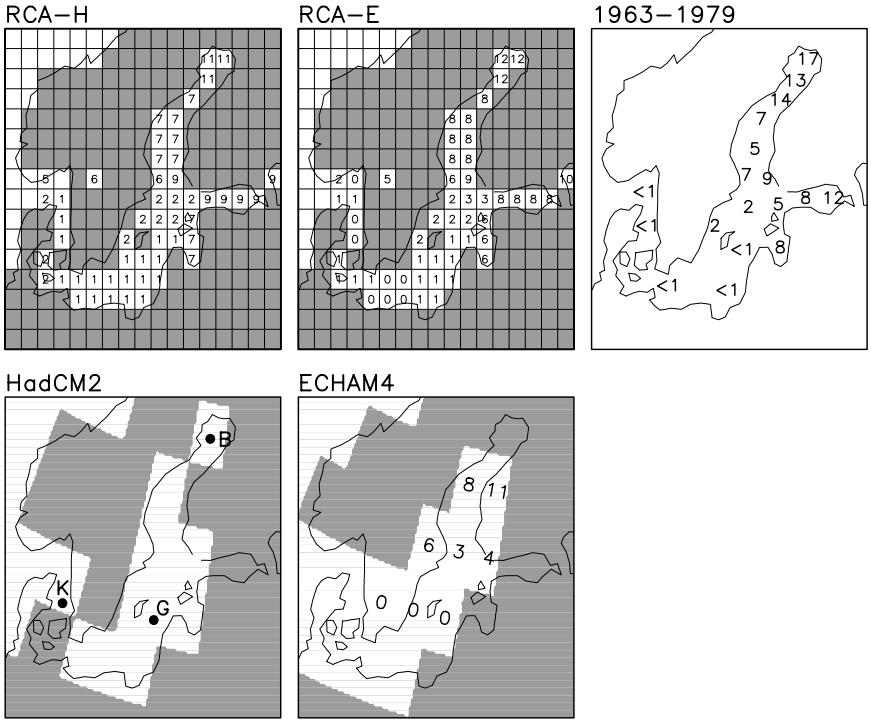

Fig. 15 Average length of the ice season (unit: 10 days) in the two RCA1 simulations, in the driving GCMs and as analyzed from 1963–1979 ice charts. *A 0* indicates that ice has been simulated, but on the average <5 days per winter; for grid boxes with no ice no value is given (HadCM2 has no ice in the Baltic Sea in the 10-year time slice). The *shading* indicates the land/sea distributions in the models (for RCA1, grid boxes with a land cover >50% are shaded). The three dots '*B*', '*G*', and '*K*' in the HadCM2 panel indicate the location of the oceanographical stations used in Fig. 16

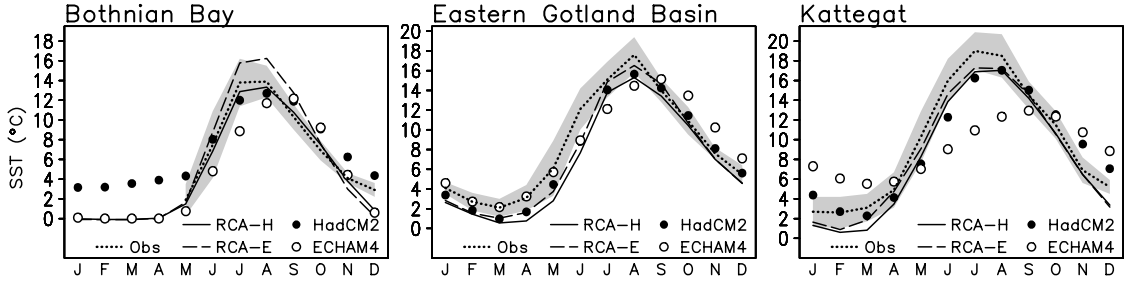

Fig. 16 Average sea surface temperature (°C) in the Bothnian Bay, the Eastern Gotland Basin and the Kattegat in RCA-H (*solid lines*), RCA-E (*dashed lines*), HadCM2 (*solid circles*) and ECHAM4 (*open circles*) and from observations (*dotted lines* and *shading* indicating ±1 interannual standard deviation)

Gotland Basin ('G') and Anholt E in Kattegat ('K'); data from Sundström 1999], the RCA1 simulations appear quite reasonable. The simulated annual SST maximum occurs correctly in July-August and the minimum in late winter. The SSTs in the Eastern Gotland Basin and the Kattegat are in most of the year slightly below the observational means. In the case of RCA-H this is consistent with the cold air temperature bias. Other possible contributors are eventual flaws in the Baltic Sea model and the general difficulty of comparing simulated basin means with point observations. In addition, the observations likely have a warm sampling bias during winter and spring because data are lacking from years with ice cover (for the same reason, no data are available in January–April for the Bay of Bothnia which in this season is regularly ice-covered in nature).

More serious problems are evident in the SSTs in the driving GCMs, taken in Fig. 16 from their closest sea grid boxes. The seasonal cycle in ECHAM4 is distorted, the annual maximum occurring in September rather than in August. This is most evident for the Kattegat, where ECHAM4 also severely underestimates the amplitude of the seasonal cycle yielding SSTs that are more typical of open ocean than to this part of the Baltic Sea. HadCM2 does a better job than ECHAM4 in the Kattegat and it also gives a fair simulation in the Eastern Gotland Basin. In the Bay of Bothnia , however, its SST in winter is close to +4 °C, rather than at the freezing point (which for the low-salt water in the Baltic Sea is slightly below 0 °C). Thus, the wintertime Baltic SSTs in HadCM2 actually increase northward. This surprising behavior might perhaps be associated with miss-functioning flux corrections.

As a result of the high SSTs, the northern parts of the Baltic Sea acquire no wintertime ice cover in HadCM2, in strong contrast with observed conditions (Fig. 15). The more southerly parts of the sea are likewise ice-free in HadCM2, but here ice is less common even in nature.

ECHAM4 has a reasonable ice climate in the Baltic Sea but the crude geography in this model prevents a detailed comparison with observations. In both RCA-H and RCA-E, the geographical distribution of ice is realistically simulated, with the longest average ice season in the Bay of Bothnia (110–120 days per year) and in the Gulf of Finland (80–90 days per year). The observational data in Fig. 15 (Swedish Meteorological and Hydrological Institute and Finnish Institute of Marine Research 1982) indicate a somewhat longer ice-season in these basins. This may be partly explained by differences in defining the ice cover. The observational estimate is based on digitized ice charts for 1963–1979, in which each $0.25° \times 0.5°$ grid box is classified as ice when the subjectively analyzed ice concentration is at least 10%. For the model runs, a linear treatment of fractional ice-cover is used (e.g., a monthly average ice concentration of 0.5 is interpreted as 15 ice days). In addition, since the whole Bay of Bothnia and the Gulf of Finland are treated as single basins, the lengthening of the ice season towards the inner parts of these cannot be resolved.

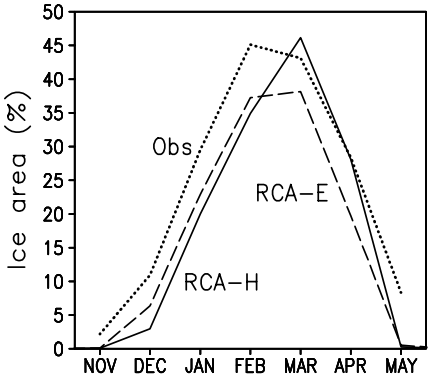

Fig. 17 10-year monthly mean Baltic Sea ice area (% of a total of $\sim$ 420 000 km^2) in RCA-H (*solid*) and RCA-E (*dashed*), and from ice charts 1963–1979 (*dotted*)

The seasonal cycle of the ice cover over the whole Baltic Sea is compared between RCA-H, RCA-E and observations in Fig. 17. There is seemingly somewhat too little ice in the simulations, excluding RCA-H in March. Although this difference is affected by the difference in the definition of ice cover, the total disappearance of ice by the end of April in the simulations indicates that the melting in spring is likely too efficient. Otherwise, the simulated seasonal cycle is in qualitative agreement with observations. The largest difference between RCA-H and RCA-E, the more abundant ice cover in the former in March–April, is explained by its colder springs.

4.4.2 Inland lakes

A comparison between the simulated and observed ice conditions in Swedish lakes is given in Fig. 18. The observed average ice season length in 37 lakes (Eklund 1999) and mean annual maximum ice thickness in 23 lakes (Eklund 1998) are compared with similar statistics for the RCA-H and RCA-E simulations. The observational data cover lakes of widely varying size but are mostly for relatively large lakes (medium area about 30 km^2). HadCM2 and ECHAM4 have no subgridscale lakes and are therefore not included in Fig. 18.

There is a reasonable agreement between the model runs and the observations in both parameters, although with relatively large differences in the case of some individual lakes. Part of this is due to the fact that ice conditions (in particular, time of freezing) depend on lake size and depth (Eklund 1999). The gridbox scale model data, which represent a weighted average over different types of lakes within the gridbox, are not necessarily representative for the individual lakes in the observational data. On the whole, there does not appear to be any systematic bias in the simulated maximum ice thickness. The length of the simulated ice season is typically somewhat short.

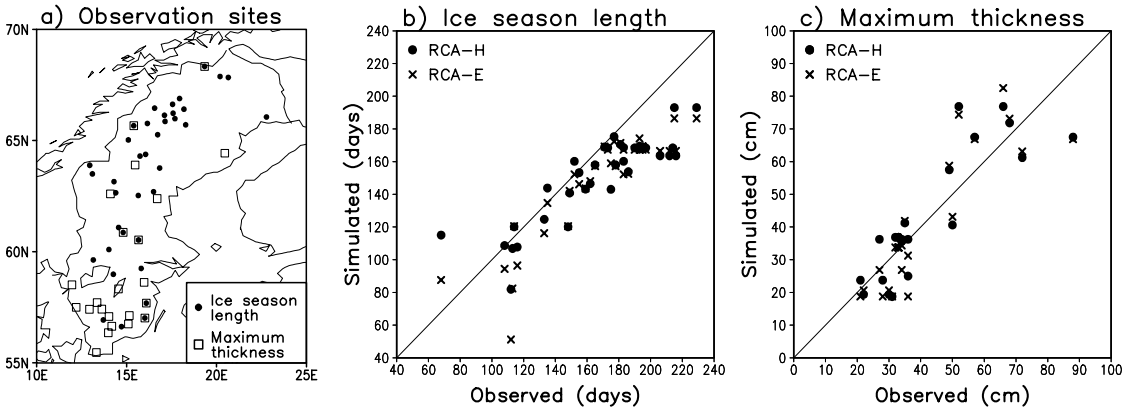

Fig. 18a–c Comparison between simulated and observed ice conditions in Swedish lakes. **a** Shows the locations of the 37 lakes with observations of average ice season length (*solid circles*) and 23 lakes with observations of mean annual ice thickness (*boxes*). Scatter diagrams between the average observed and average simulated ice season length and maximum thickness are given in **b** and **c**, respectively (*solid circles* for RCA-H and *crosses* for RCA-E)

Averaging over the 37 observed lakes, RCA-H (RCA-E) underestimates the length of the ice season by 17 (21) days. The freezing occurs too late, on the average by 11 (9) days in RCA-H (RCA-E), and the melting too early, by 6 (11) days in RCA-H (RCA-E). The late freezing may be partly explained by a warm bias in the simulated air temperatures in early winter (see Fig. 10). The early melting indicates an inconsistency, as it occurs even in RCA-H with the distinctly too cold springs. The inconsistency is at least partly due to the low ice albedo prescribed.

The idea of too efficient melting is supported by the fact that the ice melts too early without a systematic bias in its maximum thickness. It should be noted that the thickness data are for a largely different sample of lakes (mainly in southern Sweden; see Fig. 18a) than the data for ice season length (mainly northern Sweden), but this does not seem sufficient to explain the discrepancy. By contrast, the combination of reasonable maximum ice thickness with too late freezing is not necessarily physically inconsistent, since observations for Swedish lakes indicate the maximum ice thickness to be only relatively weakly affected by the time of freezing (Eklund 1998).

5 Summary with conclusion

This work describes the Rossby Centre regional Atmospheric model, RCA1, a new regional climate modeling tool building on a limited area forecast model. RCA1 now includes a more climate-oriented land surface scheme and interactive models for inland lake systems and for the Baltic Sea. First such RCA1 coupled regional simulations, forced by 10-year time slices from two GCMs, are presented as a first step in creating regional climate change scenarios for northern Europe. The main findings are summarized:

1. Some aspects of the present surface climate are simulated well in the RCA1 experiments whereas others are less faithfully reproduced. The shortness of the simulations is likely to explain some of the biases, but statistically significant biases are generally more frequent than expected from pure chance. Some of the biases (e.g., too abundant precipitation in spring and too weak meridional MSLP gradient across Scandinavia in winter) are at least qualitatively similar in the two experiments. Others differ more markedly between them. For example, the spring and summer temperatures are, on average, about 2 °C too cold in RCA-H but close to or slightly above those observed in RCA-E.

2. The large-scale biases in MSLP, tropospheric temperatures, surface air temperature and precipitation are in most aspects very similar between RCA1 and the driving GCMs. No systematic tendency of RCA1 to either amplify or reduce the biases already in the GCMs is found. However, RCA1 has a generally colder troposphere than the GCMs, with largest differences between RCA-E and ECHAM4 in summer. Differences in radiative transfer, either due to the different radiation schemes or differences in meteorological factors (and to a small extent the slightly higher greenhouse gas concentrations in ECHAM4), appear to contribute.

3. ECHAM4 has, in terms of relative humidity, a generally drier troposphere than HadCM2. This leads to a serious lack of boundary zone precipitation in RCA-E whereas no such problem occurs in RCA-H. In the inner part of the model area, the relative humidities in the two RCA1 simulations are distinctly closer to each other than those in the two GCMs, indicating that this parameter adjusts quite rapidly in RCA1. These results emphasize that, although a regional model does not necessarily need to attain its parametrizations from the driving GCM, the lateral boundaries should be placed sufficiently far away from the area of interest.

4. Even at the 88 km grid box scale, the rms differences between RCA1 and the driving GCM are typically smaller than the rms errors of the driving GCMs themselves. This is most clearly the case with upper tropospheric temperatures and MSLP in winter, but in most seasons qualitatively true even for surface air temperature and precipitation. This implies that a substantial improvement of regional simulations will require improvements even in the driving GCMs. Nevertheless, after removing the impact of the area mean biases, both the two RCA1 simulations show generally smaller errors in their distribution of surface air temperature and precipitation than the driving GCMs. Thus, RCA1 is able to add realistic geographic detail to the simulated surface climate.

5. An important improvement in RCA1 over the GCMs is the simulation of the Baltic Sea and the inland lake systems. The two GCMs have large seasonal SST biases on their Baltic Sea points, and the Baltic Sea is devoid of ice in one of them. These GCMs have no inland lakes. By contrast, the Baltic Sea model in RCA1 gives a reasonable simulation of the SST and ice conditions. (In our earlier attempts to drive RCA with the HadCM2 Nordic region SSTs the regional simulation became very unrealistic, due to the lack of ice in winter and the biased SSTs, see Rummukainen et al. 1999.) The mean annual maximum ice thickness in Swedish lakes is also found to be fairly well simulated, although the length of the ice season appears somewhat too short. Some of the latter is likely due to the chosen ice albedo value.

Regional climate modeling needs to address the issue of uncertainties in the scenarios that are produced, including uncertainties due to the choice of the driving GCM, to the regional model deficiencies and to natural climate variations present in both the GCMs and the RCMs. Solutions to these are particularly important because the RCM results will be used in impact studies. Studies with an RCM forced by more than one GCM should prove helpful in separating between biases imposed by the GCM and by the regional model parametrizations. Further such studies will be conducted with the RCA1.

The overall control simulation results suggest that RCA1 is a suitable platform for regional climate change scenarios, though further development is also required. In the near future, the present RCA1 moist physics and turbulence will be replaced by schemes developed particularly for high-resolution modeling. Whether the present 1.5-dimensional model for the Baltic Sea is sufficient for the aims of SWECLIM will be explored by coupling RCA1 also with a 3-dimensional regional ocean model (Meier et al. 1999).

Acknowledgements The SWECLIM program and the Rossby Centre are funded by MISTRA and by SMHI. The HadCM2 data were provided by the Hadley Centre. The ECHAM4 data were provided by the Max Planck Institute for Meteorology in Hamburg and the Deutsches Klimarechenzentrum (DKRZ). The latter data management benefited from cooperation with the Norwegian RegClim project. RCA1 has been run on the Cray T3E at the Swedish National Supercomputing Centre.

References

Bergström S, Graham LP (1998) On the scale problem in hydrological modelling. J Hydrol 211: 253–265

Christensen JH, Machenhauer B, Jones RG, Schär C, Ruti PM, Castro M, Visconti G (1997) Validation of present-day regional climate simulations over Europe: LAM simulations with observed boundary conditions. Clim Dyn 13: 489–506

Christensen OB, Christensen JH, Machenhauer B, Botzet M (1998) Very high-resolution regional climate simulations over Scandinavia – present climate. J Clim 11: 3204–3229

Clapp RB, Hornberger GM (1978) Empirical equations for some hydraulic properties. Water Resources Res 14: 601–604

Davies HC (1976) A lateral boundary formulation for multi-level prediction models. Q J R Meteorol Soc 102: 405–418

Dickinson RE, Errico RM, Giorgi F, Bates GT (1989) A regional climate model for the western United States. Clim Change 15: 383–422

Eerola K, Salmond D, Gustafsson N, Garcia-Moya J-A, Lönnberg P, Järvenoja S (1997) A parallel version of the HIRLAM forecast model: strategy and results. In: Hoffmann G-R, Kreitz N (eds) Making its mark. Proc 7th ECMWF Workshop on the use of Parallel Processors in Meteorology. Reading, UK, November, 1996, pp 134–143

Eklund A (1998) Istjocklek på sjöar – en statistisk bearbetning av SMHIs mätningar (Thickness of lake ice – a statistical analysis of measurements made by SMHI; in Swedish). SMHI Hydrologi 76, SMHI, SE-60176 Norrköping, Sweden, pp 19 + 9

Eklund A (1999) Isläggning och isslossning i svenska sjöar (Freezing and melting of ice in Swedish lakes; in Swedish). SMHI Hydrologi 81, SMHI, SE-60176 Norrköping, Sweden, pp 18 + 6

Elo A-R (1994) A sensitivity analysis of a temperature model of a lake examining components of the heat balance. Geophysica 30: 79–92

Geleyn JF (1987) Use of a modified Richardson for parameterizing the effect of shallow convection. J Meteorol Soc Japan, Special NWP Symposium Issue, pp 141–149

Gibson JK, Kållberg P, Uppala S, Hernandez A, Nomura A, Serrano E (1997) ERA description. ECMWF Reanalysis Project Rep Ser 1, European Centre for Medium-Range Weather Forecasts, Reading, United Kingdom, pp 66

Giorgi F, Bates GT (1989) On the climatological skill of a regional model over complex terrain. Mon Weather Rev 117: 2325–2347

Giorgi F, Mearns LO (1991) Approaches to the simulation of regional climate change: a review. Rev Geophys 29: 191–216

Giorgi F, Mearns LO (1999) Introduction to special section: regional climate modeling revisited. J Geophys Res 104: 6335–6352

Giorgi F, Marinucci MR, Bates GT (1993a) Development of a second-generation regional climate model (RegCM2). Part I: boundary-layer and radiative transfer processes. Mon Weather Rev 121: 2794–2813

Giorgi F, Marinucci MR, Bates GT, De Canio G (1993b) Development of a second-generation regional climate model (RegCM2). Part II: convective processes and assimilation of lateral boundary conditions. Mon Weather Rev 121: 2814–2832

Giorgi F, Brodeur CS, Bates G (1994) Regional climate change scenarios over the United States produced with a nested regional climate model. J Clim 7: 375–399

Gustafsson N, Nyberg L, Omstedt A (1998) Coupling of a high-resolution atmospheric model and an ocean model for the Baltic Sea. Mon Weather Rev 126: 2822–2846

Hibler WD (1979) A dynamic thermodynamic sea ice model. J Phys Oceanogr 9: 817–846

Hoskins BJ, Hsu HH, James IN, Masutani M, Sardesmukh PD, White GH (1989) Diagnostics of the global atmospheric circulation based on ECMWF analyses 1979–1989. WCRP Rep 27, pp 217 (available from WMO/WCRP, 41 Avenue Giuseppe-Motta, 1211 Geneva 2, Switzerland)

Houghton JT, et al (1996) Climate change 1995. The science of climate change. Cambridge University Press, Cambridge, UK pp 572

Hulme M, Conway D, Jones PD, Jiang T, Zhou X, Barrow EM, Turney C (1995) A 1961–90 gridded surface climatology for Europé, pp 51 + maps. (Available from Climatic Research Unit, Norwich)

Jacob D, Podzun R (1997) Sensitivity studies with the regional climate model REMO. Meteorol Atmos Phys 63: 119–129

Johns TC, Carnell RE, Crossley JF, Gregory JM, Mitchell JFB, Senior CA, Tett SFB, Wood RA (1997) The second Hadley Centre coupled ocean-atmosphere GCM: model description, spinup and validation. Clim Dyn 13: 103–134

Jones RG, Murphy JM, Noguer M (1995) Simulation of climate change over Europe using a nested regional-climate model. I: assessment of control climate, including sensitivity to location of lateral boundaries. Q J R Meteorol Soc 121: 1413–1449

Jones RG, Murphy JM, Noguer M, Keen AB (1997) Simulation of climate change over Europe using a nested regional-climate model. II: comparison of driving and regional model responses to a doubling of carbon dioxide. Q J R Meteorol Soc 123: 265–292

Kuo HL (1965) On the formation and intensification of tropical cyclone through latent heat release by cumulus convection. J Atmos Sci 22: 40–63

Kuo HL (1974) Further studies of the parametrization of the influence of cumulus convection on large-scale flow. J Atmos Sci 31: 1232–1240

Källén E (ed) (1996) HIRLAM documentation manual. System 2.5. pp 178 + pp 55 Appendix

Laine V, Heikinheimo M (1996) Estimation of surface albedo from NOAA AVHRR data in high latitudes. Tellus 48A: 424–441

Laprise R, Caya D, Giguère M, Bergeron G, Côté H, Blanchet J-P, Boer GJ, McFarlane NA (1998) Climate and climate change in western Canada as simulated by the Canadian regional climate model. Atmosphere-Ocean 36: 119–167

Levitus S, Boyer TP (1994) World ocean atlas 1994, volume 4: temperature. NOAA ATLAS NESDIS 4, pp 117

Lindström G, Gardelin M, Johansson B, Bergström S (1997) Development and test of the distributed HBV-96 hydrological model. J Hydrol 201: 272–288

Ljungemyr P, Gustafsson N, Omstedt A (1996) parametrization of lake thermodynamics in a high resolution weather forecasting model. Tellus 48A: 608–621

Louis JF (1979) A parametric model of vertical eddy fluxes in the atmosphere. Bound Lay Met 17: 187–202

Machenhauer B, Windelband M, Botzet M, Jones RG, Déqué M (1996) Validation of present-day regional climate simulations

over Europe: nested LAM and variable resolution global model simulations with observed or mixed layer ocean boundary conditions. Max-Planck-Institut für Meteorologie, Rep 191, Hamburg, pp 25 + figures and tables
Machenhauer B, Windelband M, Botzet M, Christensen JH, Déqué M, Jones RG, Ruti PM, Visconti G (1998) Validation and analysis of regional present-day climate and climate change simulations over Europe. Max-Planck-Institut für Meteorologie, Rep 275, Hamburg, pp 87 + figures and tables
McCumber M, Pielke R (1981) Simulation of the effects of surface fluxes of heat and moisture in a mesoscale numerical model. I. Soil layer. J Geophys Res 86: 9929–9938
McGregor JL (1997) Regional climate modeling. Meteorol Atmos Phys 63: 105–117
McGregor JL, Walsh K (1994) Climate change simulations of Tasmanian precipitation using multiple nesting. J Geophys Res 99: 20 889–20 905
Meier HEM, Döscher R, Coward AC, Nycander J, Döös K (1999) RCO – Rosby Centre regional ocean climate model: model description (version 1.0) and first results from the hindcast period 1992/93. Reports Oceanography 26, pp 102 SMHI, Norrköping, Sweden
Noguer M, Jones R, Murphy J (1998) Sources of systematic errors in the climatology of a regional climate model over Europe. Clim Dyn 14: 691–712
Noilhan J, Planton S (1989) A simple parametrization of land surface processes for meteorological models. Mon Weather Rev 117: 536–549
Oberhuber JM (1993) Simulation of the Atlantic circulation with a coupled sea ice-mixed layer-isopycnal general circulation model. 1: model description. J Phys Oceanogr 22: 808–829
Omstedt A (1984) A forecast model for water cooling in the Gulf of Bothnia and Lake Vänern. Report RHO 36, SMHI, SE-60176 Norrköping, Sweden
Omstedt A (1999) Forecasting ice on lakes, estuaries and shelf seas. In: Wettlaufer JS, Dash JG, Untersteiner N (eds) Ice physics in the natural and endangered environment. NATO ASI Vol I 56, Springer, Berlin Heidelberg, pp 185–208
Omstedt A, Axell LB (1998) Modeling the seasonal, interannual, and long-term variations of salinity and temperature in the Baltic proper. Tellus 50A: 637–652
Omstedt A, Nyberg L (1996) Response of Baltic Sea ice to seasonal, interannual forcing and climate change. Tellus 48A: 644–662
Omstedt A, Rutgersson A (2000) Closing the water and heat cycles of the Baltic Sea. Meteorol Z 9: 57–64
Raab B, Vedin H (eds) (1995) Climate, lakes and rivers. National Atlas of Sweden, vol 14, pp 176
Roeckner E, Arpe K, Bengtsson L, Christoph M, Claussen M, Dümenil L, Esch M, Giorgetta M, Schlese U, Schulzweida U (1996a) The atmospheric general circulation model ECHAM-4: Model description and simulation of present-day climate. Max-Planck-Institut für Meteorologie, Rep 218, Hamburg, Germany, pp 90
Roeckner E, Oberhuber JM, Bacher A, Christoph M, Kirchner I (1996b) ENSO variability and atmospheric response in a global coupled atmosphere-ocean GCM. Clim Dyn 12: 737–754
Roeckner E, Bengtsson L, Feichter J, Lelieveld J, Rodhe H (1999) Transient climate change simulations with a coupled atmosphere-ocean GCM including the tropospheric sulfur cycle. J Clim 12: 3004–3032
Rummukainen M (1997) Methods for statistical downscaling of GCM simulations. Reports Meteorology and Climatology 80, SMHI, SE-60176 Norrköping, Sweden, pp 29
Rummukainen M, Räisänen J, Ullerstig A, Bringfelt B, Hansson U, Graham P, Willén U (1998) RCA – Rossby Centre regional Atmospheric climate model: model description and results from the first multi-year simulation. Reports Meteorology and Climatology 83, SMHI, SE-60176 Norrköping, Sweden, pp 76
Rummukainen M, Räisänen J, Ullerstig A, Bringfelt B (1999) A regional climate simulation stressing the significance of the Baltic Sea ice and lake ice in the Nordic climate (change). In: Ritchie H (ed) Research activities in atmospheric and oceanic modelling, CAS/JSC working group on numerical experimentation. Rep 28, WMO/TD- 942, pp 7.60–7.61
Räisänen J (2000) CO_2-induced climate change in northern Europe: comparison of 12 CMIP2 experiments. Reports Meteorology and Climatology 87, SMHI, SE-60176 Norrköping, Sweden, pp 59
Räisänen J, Döscher R (1999) Simulation of present-day climate in Northern Europe in the HadCM2 OAGCM. Reports Meteorology and Climatology 84, SMHI, SE-60176 Norrköping, Sweden, pp 37
Räisänen P, Rummukainen M, Räisänen J (2000) Modification of the HIRLAM radiation scheme for use in the Rossby Centre regional atmospheric climate model. Department of Meteorology, University of Helsinki, Rep 49, pp 71
Sahlberg J (1988) Modelling the thermal region of lake during the winter season. Cold Region Sci Technol 15: 151–159
Sasaki H, Kida H, Koide T, Chiba M (1995) The performance of long-term integrations of a limited area model with the spectral boundary coupling method. J Meteorol Soc Japan 73: 165–181
Sass BH, Rontu L, Räisänen P (1994) HIRLAM-2 radiation scheme: documentation and tests. HIRLAM Technical Rep 16, SMHI, SE-60176 Norrköping, pp 43
Savijärvi H (1990) Fast radiation parametrization schemes for mesoscale and short-range forecast models. J Appl Meteorol 29: 437–447
Simmons AJ, Burridge DM (1981) An energy and angular momentum conserving vertical finite-difference scheme and hybrid vertical coordinates. Mon Weather Rev 109: 758–766
Stigebrandt A (1987) A model for the vertical circulation of the Baltic deep water. J Phys Oceanogr 17: 1772–1785
Sundqvist H (1993) Inclusion of ice phase of hydrometeors in cloud parametrization for mesoscale and large-scale models. Beitr Phys Atmos 66: 137–147
Sundqvist H, Berge E, Kristjánsson JE (1989) Condensation and cloud parametrization studies with a mesoscale numerical weather prediction model. Mon Weather Rev 117: 1641–1657
Sundström C (1999) Oceanografiska mätningar längs svenska kusten med kustbevakningens fartyg, 1970–1997 (Oceanographical measurements along the Swedish coast 1970–1997; in Swedish). SMHI Oceanografi, Sa PM 8, SMHI, SE-60176 Norrköping, Sweden, pp 77 + 10
Svensson U (1978) A mathematical model of the seasonal thermocline. Lund Institute of Technology, Department of Water Resources Engineering, Rep 1002, Lund, Sweden
SWECLIM (1998) Regional climate simulations for the Nordic region – first results from SWECLIM. SMHI, pp 22
Swedish Meteorological and Hydrological Institute and Finnish Institute of Marine Research (1982) Climatological Ice Atlas for the Baltic Sea, Kattegat, Skagerrak and Lake Vänern (1963–1979). Sjöfartsverket, SE-60178 Norrköping, Sweden, pp 220
Viterbo P, Beljaars A, Mahfouf J-F, Teixeira J (1999) The representation of soil moisture freezing and its impact on the stable boundary layer. Q J R Meteorol Soc 125: 2401–2426